SIAM J. Applied Dynamical Systems
Vol. 12, No. 2, pp. 789–830

Multiple Geometric Viewpoints of Mixed Mode Dynamics Associated with Pseudo-plateau Bursting*

Theodore Vo†, Richard Bertram‡, and Martin Wechselberger†

Abstract. Pseudo-plateau bursting is a type of oscillatory waveform associated with mixed mode dynamics in slow/fast systems and commonly found in neural bursting models. In a recent model for the electrical activity and calcium signaling in a pituitary lactotroph, two types of pseudo-plateau bursts were discovered: one in which the calcium drives the bursts and another in which the calcium simply follows them. Multiple methods from dynamical systems theory have been used to understand the bursting. The classic 2-timescale approach treats the calcium concentration as a slowly varying parameter and considers a parametrized family of fast subsystems. A more novel and successful 2-timescale approach divides the system so that there is only one fast variable and shows that the bursting arises from canard dynamics. Both methods can be effective analytic tools, but there has been little justification for one approach over the other. In this work, we use the lactotroph model to demonstrate that the two analysis techniques are different unfoldings of a 3-timescale system. We show that elementary applications of geometric singular perturbation theory in the 2-timescale and 3-timescale methods provide us with substantial predictive power. We use that predictive power to explain the transient and long-term dynamics of the pituitary lactotroph model.

Key words. geometric singular perturbation theory, multiple timescales, mixed mode oscillations, bursting

AMS subject classifications. 37N25, 34E17, 92B25, 37M05, 37G35

DOI. 10.1137/120892842

1. Introduction.

Bursting is a type of complex oscillatory waveform commonly seen in the electrical activity of nerve and endocrine cells [34, 18, 42, 28, 43, 44]. Characterized by alternating periods of fast spiking in the active (depolarized) phase and quiescence during which the cell is repolarized, bursts are typically more efficient than spikes in evoking hormone and neurotransmitter release [33, 48]. Characteristics of the burst pattern such as frequency and duration determine how much calcium enters the cell, which in turn determines the level of hormone secretion [59]. One particular type of bursting that has been the focus of recent modeling efforts is pseudo-plateau bursting, which features small amplitude oscillations or spikes in the active phase superimposed on relaxation type oscillations [51, 47, 39, 56]. Pseudo-plateau bursts are distinguished from plateau bursts, which feature large amplitude fast spiking in the active phase [40, 4, 32, 57].

Using geometric singular perturbation theory [19, 26], the authors showed that the pseudo-

*Received by the editors September 9, 2012; accepted for publication (in revised form) by H. Osinga March 21, 2013; published electronically May 21, 2013.
http://www.siam.org/journals/siads/12-2/89284.html
†School of Mathematics and Statistics, University of Sydney, Sydney NSW, Australia (theodore.vo@sydney.edu.au, wm@maths.usyd.edu.au). The first author's research was partially supported by an A.E. and F.A.Q. Stephens Scholarship and a Philipp Hofflin International Research Scholarship (University of Sydney). The third author's research was partially supported by the Australian Research Council and the Marsden Fund, New Zealand.
‡Department of Mathematics and Programs in Neuroscience and Molecular Biophysics, Florida State University, Tallahassee, FL 32306 (bertram@math.fsu.edu). This author's research was supported by NSF grant DMS 1220063.

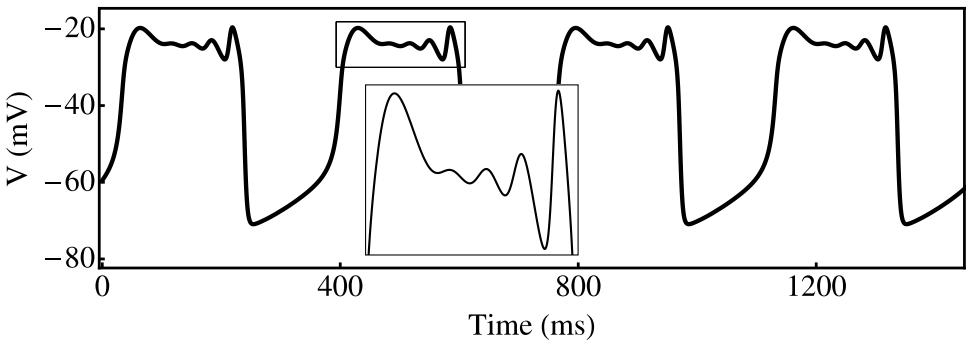

Figure 1. *A typical* 1^4 *MMO generated by a system of the type* (1.1).

plateau bursting that arose in a pituitary cell model [60, 53] was a canard-induced mixed mode oscillation (MMO) [9, 8]. MMOs are oscillatory trajectories in which there is an alternation between large amplitude and small amplitude spiking (Figure 1). A prototypical MMO is composed of L large amplitude oscillations followed by s small amplitude oscillations. This is denoted L^s and called the MMO signature. A general MMO pattern, then, is just a concatenation of these MMO units resulting in a signature $L_1^{s_1} L_2^{s_2} \dots L_n^{s_n}$.

A vital feature of the analysis of MMOs is the multiple timescale structure of the governing system (see [14] for an extensive overview). In this work, we focus on MMOs in 3-timescale systems of the form

$$\begin{aligned} \varepsilon \dot{x} &= f(x, y, z), \\ \dot{y} &= g(x, y, z), \\ \dot{z} &= \delta h(x, y, z), \end{aligned} \tag{1.1}$$

where ε, δ are small, independent parameters and f, g, and h are sufficiently smooth functions. The variables (x, y, z) vary over different timescales with $x \in \mathbb{R}^m$ classified as fast, $y \in \mathbb{R}^n$ classified as intermediate, and $z \in \mathbb{R}^k$ classified as slow. Such 3-timescale systems have received little attention [25, 28, 29] and are typically treated as 2-timescale problems, which is the natural setting for geometric singular perturbation theory. However, the presence of two perturbation parameters means that there are various ways in which the theory can be implemented. One particular implementation uses ε as the singular perturbation parameter while keeping δ fixed. System (1.1) is then partitioned into a fast subsystem described by the x dynamics and a slow subsystem described by the (y, z) dynamics. Another viewpoint of (1.1) utilizes δ as the singular perturbation parameter with ε fixed, creating a family of fast (x, y) subsystems parametrized by the slow variable z.

This asymptotic approach with perturbation parameter δ is the standard approach to bursting oscillations [40, 41] in systems (1.1) with a single slow variable z [4, 32, 6, 51, 57, 47]. Bursts are classified according to the fast (x, y) subsystem bifurcations (with respect to z) involved in the initiation/termination of the active phase [41, 24]. Plateau and pseudo-plateau bursting in particular feature a Hopf bifurcation of the fast subsystem in the active phase, the criticality of which distinguishes the two bursting types [39, 56]. In the plateau case, the Hopf is supercritical and the large amplitude active phase spikes are related to stable

periodic orbits of the fast subsystem. In the pseudo-plateau case, the small amplitude spikes are transient oscillations generated by unstable limit cycles emanating from a subcritical Hopf [47]. Note that plateau and pseudo-plateau bursting can be converted into one another via parameter changes that alter the criticality of the fast subsystem Hopf [39, 54]. Plateau bursting and various features of pseudo-plateau bursting, such as resetting properties [47] and burst termination due to fast subsystem manifolds [38], are well understood in the classic approach.

More recent studies of pseudo-plateau bursting [60, 53, 52] make use of ε as the perturbation parameter and complement the classic slow/fast analysis. Key organizing structures are the fast x subsystem equilibria and singularities of the slow (y, z) subsystem. Hyperbolic equilibria of the fast subsystem, parametrized by the slow variables, approximate attracting and repelling slow manifolds. The extension of these manifolds by the flow into nonhyperbolic regions gives rise to complex phenomena. In particular, transverse intersections of these slow manifolds (canard solutions) shape the dynamics [11, 49, 62]. The theory of canard-induced MMOs [9] then provides the theoretical basis for understanding burst phenomena such as the transition from spiking (relaxation oscillations) to bursting (MMOs) and how spike-adding bifurcations can occur. The two slow/fast analysis techniques yield key insights into the mixed mode dynamics of pseudo-plateau bursting. Comparative analyses of the two slow/fast methods have been performed (for instance, in [53]); however, there have been few attempts to reconcile these approaches [52] in the context of (1.1).

There are multiple goals to our study. First and foremost, we wish to broaden the scope of geometric singular perturbation theory by showing that elementary applications of the theory can be a powerful analytical tool in understanding 3-timescale problems. We compare the familiar 2-timescale methods with a 3-timescale analysis and demonstrate the efficacy of each technique. In conjunction with this, we illustrate our assertions by analyzing a 3-timescale, four-dimensional (4D) pituitary lactotroph model [51, 55] and show that our multiple geometric viewpoints provide a fairly complete view of the dynamics. Physiologically, we are motivated by a desire to understand a complex neuroendocrine model. Mathematically, we are interested in the relationship between multiple analytical techniques. Our work complements the work of [52], in which the relationship between geometric features of the 2-fast/1-slow and 1-fast/2-slow analysis techniques is demonstrated in a three-dimensional (3D) version of the pituitary lactotroph model. We take a mostly expository and heuristic approach.

The outline of the paper is as follows: in section 2, we describe the pituitary lactotroph model and briefly survey the work on it to date. We show, via dimensional analysis, that our model belongs to the class of systems (1.1). In section 3, we investigate the bifurcation structure of our model and identify the regions in parameter space where MMOs exist. Sections 2 and 3 serve as a preamble to the main results, which are presented in sections 4, 5, and 6. Section 4 details a slow/fast analysis in which there is one fast variable and three slow variables, examples of which are currently scarce [22, 23]. We then recall the standard slow/fast analysis in section 5, where everything is treated as fast except for a single slow variable. The crux of our work lies in section 6, where we perform a geometric singular perturbation analysis of the full 3-timescale problem (1.1). We formulate our 3-timescale analysis in a general way to emphasize that our approach can easily be adapted to other 3-timescale problems. We show that the 3-timescale decomposition inherits the strengths of the 2-timescale methodologies,

affording us a remarkable degree of control and predictive power. Sections 4, 5, and 6 highlight an unusual degeneracy about which the small oscillations of the MMOs are localized. In section 7, we examine this degeneracy more closely while comparing the three analytical approaches. We then conclude in section 8 with a discussion.

2. The mathematical model. We consider a 4D conductance-based model for the electrical activity and calcium signaling in a pituitary lactotroph [51]. The model variables are the membrane potential V of the cell, the fraction n of activated K^+ channels of the delayed rectifier type, the fraction e of A-type K^+ channels that are not inactivated, and the cytosolic-free Ca^{2+} concentration c. The equations are

$$\begin{aligned} C_m \frac{dV}{dt} &= -\left(I_{Ca} + I_K + I_{BK} + I_{SK} + I_A\right), \\ \frac{dn}{dt} &= \frac{\lambda}{\tau_n}(n_\infty(V) - n), \\ \frac{de}{dt} &= \frac{1}{\tau_e}(e_\infty(V) - e), \\ \frac{dc}{dt} &= -f_c\left(\alpha I_{Ca} + k_c c\right), \end{aligned} \tag{2.1}$$

where I_{Ca} is an inward Ca^{2+} current, I_K is an outward delayed rectifying K^+ current, I_{BK} is a fast-activating large-conductance BK-type K^+ current, I_{SK} is a small Ca^{2+}-activated K^+ current, and I_A is an A-type K^+ current. The currents are defined by

$$\begin{aligned} I_{Ca} &= g_{Ca} m_\infty(V)(V - V_{Ca}), \\ I_K &= g_K n(V - V_K), \\ I_{BK} &= g_{BK} f_\infty(V)(V - V_K), \\ I_{SK} &= g_{SK} s_\infty(c)(V - V_K), \\ I_A &= g_A a_\infty(V) e(V - V_K). \end{aligned}$$

The main parameters of interest are the maximal conductance of delayed rectifier K^+ channels g_K, the maximum conductance of BK-type K^+ channels g_{BK}, and the maximal conductance of A-type K^+ channels g_A. Details of the steady state functions and system parameters are provided in Appendix A.

The pituitary lactotroph model (2.1) is capable of generating pseudo-plateau bursting (MMOs) over a range of parameter values. In most endocrine cell bursting models, the bursting oscillations are driven by the slow, systematic variation in the calcium concentration [32, 51, 57, 65]. Changes in the intracellular calcium concentration play a crucial role in the functioning of almost every cell type [27]. When the intracellular calcium concentration is fixed, the bursting ceases (Figure 2(a)). This is referred to in [55] as classic bursting. Unexpectedly there are instances where the pseudo-plateau bursting persists almost unaltered when the calcium concentration is fixed [55] (Figure 2(b)). This is unusual since the slow variation of the intracellular calcium concentration is typically responsible for clustering impulses into episodes of electrical activity. We dub MMOs driven by the calcium fluctuations *dynamic* MMOs. We call those MMOs that do not require the calcium fluctuations *calcium-conducting*

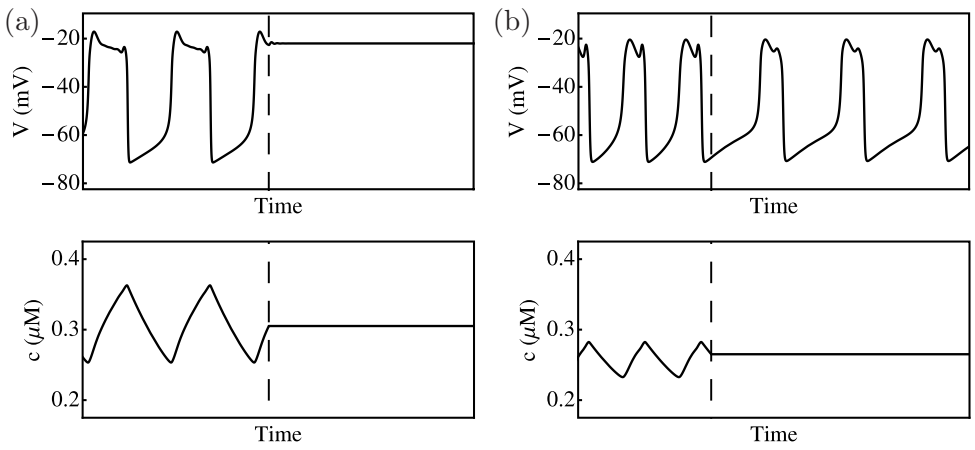

Figure 2. *Time traces of the electrical activity and calcium concentration in* (2.1) *for* (a) *classic bursting (dynamic MMOs), in which the slow changes in the calcium concentration drive the bursts, and* (b) *"novel" bursting (calcium-conducting MMOs), in which the calcium concentration is not driving the bursts but simply follows them. The parameters were set at* $C_m = 2$ pF, $f_c = 0.01$, $g_{BK} = 0.4$ nS, $g_A = 10$ nS, *and* (a) $g_K = 4$ nS *or* (b) $g_K = 6$ nS. *The vertical dashed line marks the instant at which the calcium is fixed.*

MMOs. Here, we use "conducting" in the sense that the calcium oscillations follow the bursts rather than drive them.

The discovery of dynamic and calcium-conducting MMOs in [55] marked the juncture at which studies of the pituitary lactotroph model diverged. Early treatments of (2.1) focused on the calcium-conducting MMOs since they were novel. To study these calcium-conducting MMOs a 3D model reduction, in which all nonessential elements (including the calcium concentration) were removed, was introduced [55]. Detailed analysis of these calcium-conducting MMOs was then performed [60, 61]. However, due to the physiological importance of calcium oscillations, attention was eventually given again to the dynamic MMOs. A 3D reduction of (2.1) in which the hyperpolarizing A-type current was absent was used to study the dynamic MMOs [53]. In both cases, the theory of canard-induced MMOs showed that the pseudo-plateau bursting arose from canard dynamics. In spite of these advances, the two 3D reductions of (2.1) remain as fairly separate entities. There has been virtually no work done to reconcile the results from the two 3D reductions and form a coherent picture. In this work, we tie the various threads from [51, 55, 60, 53, 61] and provide a first step towards a unified picture of the dynamics of (2.1).

To facilitate our analysis, we first perform a dimensional analysis of (2.1). The variables (V, n, e, c) vary on different timescales. To see this, we introduce a dimensionless timescale $t_I = t/k_t$ with reference timescale $k_t = \tau_e$, transforming (2.1) to

$$\begin{aligned} \frac{C_m}{g_{\max} k_t}\frac{dV}{dt_I} \equiv \varepsilon \frac{dV}{dt_I} &= f(V, n, e, c), \\ \frac{dn}{dt_I} &= \frac{k_t}{\tau_n}(n_\infty(V) - n) \equiv g_1(V, n), \\ \frac{de}{dt_I} &= \frac{k_t}{\tau_e}(e_\infty(V) - e) \equiv g_2(V, e), \end{aligned} \tag{2.2}$$

$$\frac{dc}{dt_I} = -\frac{k_t}{(f_c k_c)^{-1}}\left(\frac{\alpha}{k_c} I_{Ca} + c\right) \equiv \delta h(V,c),$$

where $g_{\max} = 10\,\text{nS}$ is a typical conductance scale and

$$f(V,n,e,c) = -\frac{1}{g_{\max}}\left(I_{Ca} + I_K + I_{BK} + I_{SK} + I_A\right)$$

is a rescaled version of the right-hand side of the V-equation of (2.1).[1] The membrane potential V evolves on a fast timescale (given to leading order by $C_m/g_{\max} < 1$ ms), while (n,e) evolve on an intermediate timescale ($\tau_e = 20\,\text{ms}$ and $\tau_n/\lambda \approx 43\,\text{ms}$). The Ca^{2+} concentration evolves on a slow timescale ($\frac{1}{f_c k_c} = 625\,\text{ms}$). In particular, decreasing C_m increases the timescale separation between V and (n,e,c), which is reflected in the singular perturbation parameter $\varepsilon = \frac{C_m}{k_t g_{\max}} \ll 1$. Similarly, decreasing f_c increases the timescale separation between (V,n,e) and c, which is reflected in the singular perturbation parameter $\delta = k_t f_c k_c \ll 1$. We will use (ε,δ) and (C_m,f_c) interchangeably since (ε,δ) have simple linear dependences on the biophysical parameters (C_m,f_c). Thus, system (2.2) is a singularly perturbed problem with fast variable V, intermediate variables (n,e), and slow variable c and small, independent perturbation parameters ε,δ.

In its current form, system (2.2) is written such that the motions in V are $\mathcal{O}(\varepsilon^{-1})$, the motions in (n,e) are $\mathcal{O}(1)$, and the motions in c are $\mathcal{O}(\delta)$. Thus, over $\mathcal{O}(1)$ time intervals, (2.2) naturally highlights the motions in the intermediate variables (n,e). We say that (2.2) is written over an intermediate timescale. An equivalent description of the dynamics can be obtained by rescaling time ($t_I = \varepsilon\, t_F$) to obtain the fast system

$$\begin{aligned}
\frac{dV}{dt_F} &= f(V,n,e,c),\\
\frac{dn}{dt_F} &= \varepsilon\, g_1(V,n),\\
\frac{de}{dt_F} &= \varepsilon\, g_2(V,e),\\
\frac{dc}{dt_F} &= \varepsilon\,\delta\, h(V,c).
\end{aligned} \tag{2.3}$$

Alternatively, we can obtain a different viewpoint of the dynamics by rescaling time ($t_S = \delta t_I$) to give the equivalent slow system

$$\begin{aligned}
\varepsilon\,\delta\,\frac{dV}{dt_S} &= f(V,n,e,c),\\
\delta\,\frac{dn}{dt_S} &= g_1(V,n),\\
\delta\,\frac{de}{dt_S} &= g_2(V,e),\\
\frac{dc}{dt_S} &= h(V,c).
\end{aligned} \tag{2.4}$$

[1] We avoid complete nondimensionalization, as the V and c scalings have no influence on the timescales. This also allows easy comparison with data and prior studies.

Systems (2.2), (2.3), and (2.4) stress the notion that the choice of reference scale k_t is not important. The multi-timescale structure is an intrinsic feature of the model, and (2.2), (2.3), and (2.4) simply reflect different choices of k_t.

3. Full system bifurcation analysis. The first step towards a classification of the dynamics is a full system bifurcation analysis, which complements slow/fast analysis techniques and views the MMOs as periodic solutions with complex structure [44, 56]. In [60, 53, 61], two-parameter diagrams were constructed for reductions of (2.2) that focused on calcium-conducting MMOs (with $\delta \to 0$ and c removed) or dynamic MMOs (with $g_A = 0$ nS and e decoupled) but not both. Here, we extend that work to the full 4D system.

3.1. The three conductances. In [61], the authors performed careful one-parameter bifurcation analyses of (2.2) with $\delta = 0$. We now extend the bifurcation analysis to (2.2) with $\delta \neq 0$. However, since the bifurcation structure of (2.2) is not a primary focus of this work, we highlight only the salient features for our purposes and leave more detailed discussions to future work. Using AUTO [15, 16], the bifurcation structure of the lactotroph model (2.2) was calculated for each of the three conductances g_K, g_{BK}, and g_A (Figure 3). The L_2 norm refers to either the standard Euclidean norm for equilibria or the L_2 norm for periodic orbits.

Figure 3(a) shows the bifurcation structure of (2.2) with g_K as the principal continuation parameter. Here, we are considering bifurcations that arise from variations in the repolarizing current I_K. For small g_K, the depolarized equilibrium state (labeled Dep) is attracting (black curve). The depolarized steady state loses stability at a subcritical Hopf bifurcation (denoted by HB_{g_K}) at $g_K \approx 0.576$ nS. Emanating from the Hopf point is the spiking branch (blue curve), which terminates outside the physiological domain at another subcritical Hopf point. The $s = 1$ bursting branch (red) connects with the spiking branch at period doubling (PD) points, where s denotes the number of small oscillations in the MMO. The $s = 2$ branch (green) is born at a saddle node (SN) of periodics at $g_K \approx 0.613$ nS and is a closed isola of MMOs. The bursting families $s = k$, $k > 2$ (not shown), have the same configuration as the $s = 2$ case with ever-decreasing stability plateaus. These closed isolas are all born in SN points in a neighborhood of the PD point where the spiking and first bursting branches connect (at $g_K \approx 0.617$ nS). It has been observed (numerically) that situated between the $s = k$ and $s = k+1$ ($k \geq 0$) bursting families are isolas of MMOs with signatures that are some mixture of 1^k and 1^{k+1} patterns (not shown). For additional details we refer the reader to [61], where the transitions between MMO families are carefully studied in system (2.2) with $\delta = 0$.

Figure 3(b) shows bifurcations of (2.2) with respect to g_{BK}, the biophysical parameter that controls the BK current and reliably increases c (with increasing g_{BK}) [51]. The bifurcation structure of g_{BK} has a reversed orientation to the g_K bifurcation structure, but the core elements are the same. There is a curve of (depolarized) equilibria (black curve) that loses stability at a subcritical Hopf bifurcation ($\mathrm{HB}_{g_{\mathrm{BK}}}$) at $g_{BK} \approx 2.499$ nS. Spiking orbits (blue curve) arise from the Hopf bifurcation and are stable for the smallest g_{BK} values. As g_{BK} is increased from 0 nS, we encounter the various MMO families. The $s = 1$ branch (red curve) connects with the $s = 0$ branch at PD points, and the remaining bursting families are disjoint, closed curves. The isolas are born in SN points in a neighborhood of the PD point where the $s = 0$ and $s = 1$ branches connect (at $g_{BK} \approx 2.338$ nS). As before, there exist MMO families with complex signature between each bursting family.

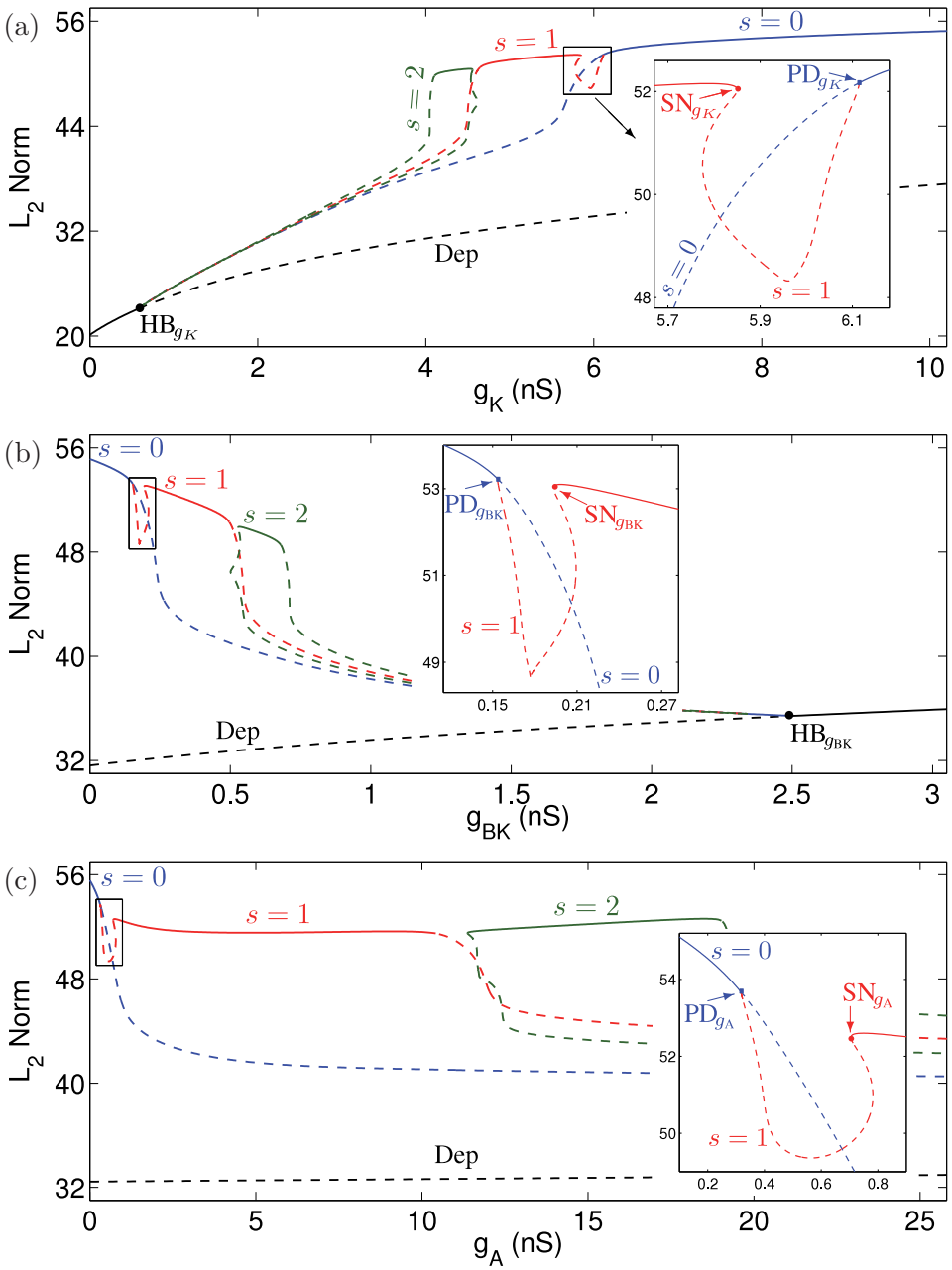

Figure 3. *One-parameter bifurcation structure of* (2.2) *with* $C_m = 2$ pF *and* $f_c = 0.01$. (a) $g_{BK} = 0.4$ nS, $g_A = 4$ nS. (b) $g_K = 5$ nS, $g_A = 4$ nS. (c) $g_K = 5$ nS, $g_{BK} = 0.4$ nS. *Stable and unstable objects are denoted by solid and dashed lines, respectively. Insets: transition between spiking and bursting branches.*

Figure 3(c) shows a bifurcation diagram of (2.2) with principal continuation parameter g_A. The bifurcations we are treating in this case are due to variations in the subthreshold current I_A. The g_A bifurcation structure is inherently different from the g_K and g_{BK} structures. In

the g_A case, there is no Hopf bifurcation. The depolarized steady state (black curve) bifurcates at a saddle node on invariant circle (SNIC) bifurcation well beyond the physiological domain (not shown), where it meets a hyperpolarized steady state. Like the g_{BK} case, the spiking orbits (blue curve) are stable for the smallest g_A values. The first bursting family (red curve) arises from the spiking branch at a PD point at $g_A \approx 0.316$ nS but terminates (at large g_A) at a homoclinic point. The remaining MMO families are disjoint but not closed. In fact, they all terminate at homoclinics far outside the physiological domain. Moreover, unlike the g_K and g_{BK} cases, there is a maximal MMO family (not shown). This maximal bursting family has the largest stability plateau and terminates at the SNIC point.

In each panel of Figure 3, there is an inset that shows the transition from the spiking branch (blue, $s = 0$) to the first bursting branch (red, $s = 1$). In each case the spiking branch loses stability at a PD point, labeled PD_{g_x}, where $x \in \{K, BK, A\}$. The $s = 1$ branch does not immediately become stable, and there is a window of complex MMO families. The $s = 1$ branch eventually becomes stable at the SN point, denoted by SN_{g_x}, with $x \in \{K, BK, A\}$. This window of complex MMOs sitting between adjacent bursting families vanishes as the perturbation parameter C_m is decreased. In fact, for sufficiently small C_m (i.e., ε), the adjacent MMO branches overlap and there is bistability (see [61]).

3.2. The bursting boundaries. Using the one-parameter diagrams (Figure 3), we can now construct two-parameter diagrams to identify the regions in parameter space where MMOs exist (Figure 4). We can also use these diagrams to see where the bursting sits relative to other types of dynamical behavior. We will only concentrate on the boundaries of the bursting behavior and save refinements of our two-parameter diagrams for future work.

In Figure 4, we show diagrams for the singular limit $(\varepsilon, \delta) \to (0, 0)$ (panels (a), (c), and (e)) but defer the discussion to section 6. Panel (b) shows the (g_K, g_{BK}) diagram for $g_A = 4$ nS, $C_m = 2$ pF, and $f_c = 0.01$. In the physiologically relevant domain, there are three distinct types of behavior: spiking, bursting, and depolarized steady states. The spiking and bursting regions are separated by the $\mathrm{PD}_{g_K}/\mathrm{PD}_{g_{\mathrm{BK}}}$ curve, which was calculated by a two-parameter continuation of the PD_{g_K} point. Equivalently, this border can be computed by continuation of the $\mathrm{PD}_{g_{\mathrm{BK}}}$ point. In any case, we choose the PD point instead of the SN point as the spiking/bursting boundary since the PD point is where the spiking branch loses stability and gives way to trajectories that are mixtures of spikes and bursts. Note that continuation of the SN point would generate essentially the same boundary. The other boundary that delimits the MMO regime is the $\mathrm{HB}_{g_K}/\mathrm{HB}_{g_{\mathrm{BK}}}$ curve, which was obtained from a two-parameter continuation of the HB_{g_K} (or $\mathrm{HB}_{g_{\mathrm{BK}}}$) point.

In Figure 4(d), $g_{BK} = 0.4$ nS, and in Figure 4(f), $g_K = 5$ nS. As in panel (b), the main types of dynamical behavior in panels (d) and (f) are spiking, bursting, and depolarization. The spiking and bursting behaviors in (d) are separated by the $\mathrm{PD}_{g_K}/\mathrm{PD}_{g_A}$ curve, and in (f) the border is the $\mathrm{PD}_{g_{\mathrm{BK}}}/\mathrm{PD}_{g_A}$ curve. Moreover, the divide between spiking and depolarization arises from continuation of the Hopf bifurcation (the $\mathrm{HB}_{g_K}/\mathrm{HB}_{g_A}$ curve in (d) and the $\mathrm{HB}_{g_{\mathrm{BK}}}/\mathrm{HB}_{g_A}$ curve in (f)). Note in Figures 4(d) and (f) that the 1D g_A slice taken in Figure 3(c) never intersects a Hopf bifurcation.

Thus, using the full system bifurcation analysis, we have identified the regions in parameter space where MMOs exist. In addition, we can deduce that the bursting waveform broadens

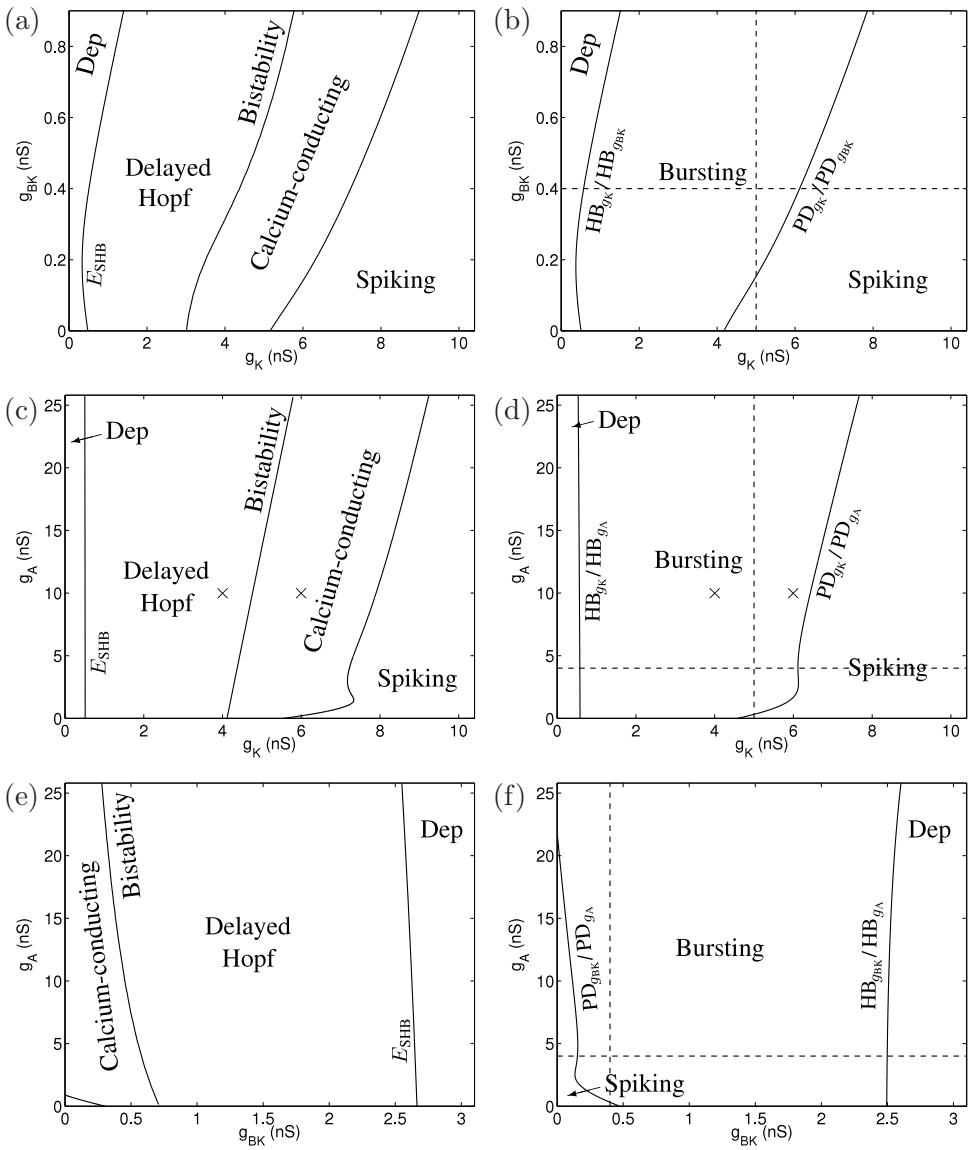

Figure 4. *Two-parameter bifurcation structure of* (2.2). *In* (a) *and* (b), $g_A = 4$ nS. *In* (c) *and* (d), $g_{BK} = 0.4$ nS. *In* (e) *and* (f), $g_K = 5$ nS. *Panels* (a), (c), *and* (e) *have* $C_m = 0$ pF *and* $f_c = 0$, *while panels* (b), (d), *and* (f) *have* $C_m = 2$ pF *and* $f_c = 0.01$. *The MMO boundaries are generated by continuing the PD and Hopf points from section* 3.1 *(see text for details). The crosses in panels* (c) *and* (d) *indicate the positions of Figures* 2(a) *and* (b). *The dashed lines denote the one-dimensional* (1D) *slices taken in Figure* 3.

$(s \to \infty)$ when the parameters approach the HB boundary. Conversely, the bursting waveform narrows $(s \to 0)$ when the spiking/bursting boundary is approached. In other words, our diagrams suggest that g_A has little effect on the number of subthreshold oscillations and that s is determined primarily by g_K and g_{BK}. We now concern ourselves with the question of the origin and properties of the MMOs. At the core of our approach is geometric singular perturbation theory.

4. The ε-viewpoint. Geometric singular perturbation theory [19, 26] is a geometric approach to multiscale systems that allows one to predict the full system dynamics based on lower-dimensional subproblems. The presence of two perturbation parameters, ε and δ, in (2.2) provides us with multiple pathways along which we may proceed. In this section we consider a timescale splitting of (2.2) in which there is only one fast variable and everything else is considered slow. Such timescale splittings have been used to effectively explain neuronal dynamics [17, 18, 43, 44, 64] and intracellular calcium dynamics [22, 23]. This section also adds to the currently sparse literature of examples dealing with systems that have more than two slow variables [22, 23, 63]. The 1-fast/k-slow approach has been applied to 3D reductions of (2.2) in which $k = 2$. The addition of a third slow variable does not significantly change the procedure.

4.1. Geometric singular perturbation analysis. For a fixed δ, system (2.2) is a singularly perturbed problem with perturbation parameter ε where V is fast and (n, e, c) are "slow." The fast system is given by (2.3), and an equivalent "slow" system is given by (2.2) (or (2.4)). Taking the singular limit $\varepsilon \to 0$ on the fast timescale t_F gives the 1D layer problem

$$\begin{aligned} \frac{dV}{dt_F} &= f(V, n, e, c), \\ \frac{dn}{dt_F} &= 0, \\ \frac{de}{dt_F} &= 0, \\ \frac{dc}{dt_F} &= 0, \end{aligned} \tag{4.1}$$

which is an approximation of (2.2) in which the "slow" processes are assumed to stand still. A different approximation can be obtained by taking the singular limit $\varepsilon \to 0$ in the "slow" system (i.e., on the intermediate timescale t_I) to give the 3D reduced problem

$$\begin{aligned} 0 &= f(V, n, e, c), \\ \frac{dn}{dt_I} &= g_1(V, n), \\ \frac{de}{dt_I} &= g_2(V, e), \\ \frac{dc}{dt_I} &= \delta h(V, c). \end{aligned} \tag{4.2}$$

In the approximation (4.2), the fast variable V is assumed to be so rapid that it adjusts instantaneously to any changes in state.

Remark 4.1. We note in (4.2) that c operates on a slower timescale than the other variables. That is, (4.2) itself is a singularly perturbed problem with δ as a small parameter. We demonstrate in this section what information can be gleaned from the 2-timescale methodology with ε as the principal perturbation parameter. In section 6, we acknowledge the full 3-timescale structure of (2.2) and show that we can use the extra timescale to our advantage to gain greater predictive power.

The aim of geometric singular perturbation theory is to concatenate the information obtained from the lower-dimensional subproblems (4.1) and (4.2) to provide a unified global description of (2.2). We start with a bifurcation analysis of the 1D layer problem (4.1). The set of critical points of (4.1) is typically called the *critical manifold*, S, defined by

$$S := \left\{(V,n,e,c) \in \mathbb{R}^4 : f(V,n,e,c) = 0\right\}. \tag{4.3}$$

If the eigenvalues of the Jacobian f_V are uniformly bounded away from the imaginary axis for some compact subset S_0 of S, we call S_0 normally hyperbolic. Fenichel theory [19, 26] is the thread that ties the singular (4.1), (4.2) and nonsingular (2.2) systems together. It guarantees that normally hyperbolic invariant manifolds of equilibria of the layer problem (4.1) persist as locally invariant slow manifolds S_ε of the full problem (2.2) for sufficiently small ε. Moreover, the restriction of the flow (2.2) to S_ε is a small smooth perturbation of the flow of the reduced problem (4.2).

For normally hyperbolic critical manifolds the geometric theory is fairly complete. However, Fenichel theory breaks down at points on the critical manifold where normal hyperbolicity is lost (such as folds of S due to a zero eigenvalue). Not surprisingly, the dynamics we are interested in are usually localized around these bifurcations. In our model system, S is a 3D folded manifold with 2D *fold surface*, L, defined as the set of equilibria of (4.1) with a zero eigenvalue:

$$L := \{(V,n,e,c) \in S : f_V(V,n,e,c) = 0\}. \tag{4.4}$$

The fold surface L divides the critical manifold S into attracting sheets S^a (where $f_V < 0$) and repelling sheets S^r (where $f_V > 0$). Solutions of (4.1) flow along the 1D fast fibers $\{(n,e,c)$ constant$\}$ towards an attracting sheet S^a or away from a repelling sheet S^r.

The critical manifold S is not only the manifold of equilibria of (4.1) but is also the phase space of the differential-algebraic system (4.2). That is, S is the interface between the layer and reduced problems, (4.1) and (4.2), respectively. A complete description of the dynamics of (4.2) is given by projection onto a slow-fast variable base, (V,e,c) say:

$$\begin{aligned} -f_V \frac{dV}{dt_I} &= f_n\, g_1(V,n) + f_e\, g_2(V,e) + \delta f_c\, h(V,c) \equiv F_\delta(V,n,e,c),\\ \frac{de}{dt_I} &= g_2(V,e),\\ \frac{dc}{dt_I} &= \delta h(V,c), \end{aligned} \tag{4.5}$$

where n satisfies (4.3). Desingularization (i.e., a rescaling in time $dt_I = -f_V\, dt_I^*$) removes the singular term at the fold and gives the *desingularized system*

$$\begin{aligned} \frac{dV}{dt_I^*} &= F_\delta(V,n,e,c),\\ \frac{de}{dt_I^*} &= -f_V\, g_2(V,e),\\ \frac{dc}{dt_I^*} &= -\delta\, f_V\, h(V,c). \end{aligned} \tag{4.6}$$

We observe that the desingularized system (4.6) is equivalent to (4.5) on the attracting sheets S^a but has opposite orientation on the repelling sheets S^r due to the time rescaling.

The desingularized system (4.6) has two kinds of singularities: ordinary and folded. Ordinary singularities are true equilibria of (2.2), defined by

$$E := \{(V, n, e, c) \in S : g_1(V, n) = g_2(V, e) = h(V, c) = 0\}. \tag{4.7}$$

The ordinary singularities are isolated points on the critical manifold. Folded singularities, on the other hand, are points along the fold surface L where the right-hand side of the V equation vanishes. That is, the curve of folded singularities M_δ is defined by[2]

$$M_\delta := \{(V, n, e, c) \in L : F_\delta(V, n, e, c) = 0\}. \tag{4.8}$$

Note that the folded singularities are special points of (4.5) where there is a cancellation of a simple zero, allowing trajectories of the reduced problem (4.5) to cross the fold L with nonzero speed. Such solutions are called singular canards [49, 62, 63], and their persistence under small perturbations can give rise to complex dynamics such as in [12, 34, 42, 43, 64].

Since there is a curve of folded singularities, the Jacobian of (4.6) evaluated along M_δ has two linearly dependent rows. Consequently, there will always be a zero eigenvalue. The eigenvector corresponding to this zero eigenvalue is tangent to M_δ. Generically, the remaining two eigenvalues have nonzero real part. We classify the folded singularities M_δ, using their nonzero eigenvalues, as equilibria of (4.6). There are three generic types: Those with real eigenvalues of opposite sign are called folded saddles. Folded singularities that have two negative (or positive) real eigenvalues are called folded nodes. Folded foci are defined as points of M_δ with complex eigenvalues.

The boundary between folded saddles and folded nodes is a degenerate singularity called folded saddle node (FSN). We are interested in the FSN points because they are the organizing centers for delay phenomena (we refer the reader to [31] for details of FSN singularities). In particular, an FSN of type II occurs when there is a transcritical bifurcation of ordinary and folded singularities. That is, the set of FSN II points is precisely the set of singular Hopf bifurcations [1, 2, 20]:

$$E_{\mathrm{SHB}} := \{(V, n, e, c) \in E : f_V(V, n, e, c) = 0\}. \tag{4.9}$$

An FSN of type I corresponds to the coalescence of a folded saddle and a folded node.

Remark 4.2. There are two ways in which an FSN I can occur in (4.6). In the first scenario, an FSN I may occur at a fold in the curve of folded singularities M_δ. Alternatively, an FSN I bifurcation is associated with the change in sign of an eigenvalue when a special curve crosses the fold surface L:

$$M_\delta^{\mathrm{I}} := \{(V, n, e, c) \in L : g_1 = \delta G_1(V, n, e, c, \delta),\ g_2 = \delta G_2(V, n, e, c, \delta)\}, \tag{4.10}$$

where the functions $G_1(V, n, e, c, \delta)$ and $G_2(V, n, e, c, \delta)$ are computable. The geometric interpretation of (4.10) will become clear in section 6.1, where we make use of the full 3-timescale machinery.

[2]The δ subscript in F_δ and M_δ is a notational convenience used to indicate the δ dependence and does not denote a derivative.

Both FSN singularities are common in applications. FSN II singularities have been identified in several neural models [43, 44, 53, 60] and are recognized as mechanisms for MMOs [20]. FSN I singularities have turned up, for instance, in the forced van der Pol oscillator [50], where they mark the onset of complex and chaotic dynamics. More recently, FSN I points have been observed in the 3D reduction of (2.2) in which the A-type current is removed [53].

4.2. Singular orbits and canards. As we saw in section 3.2, the attractor of system (2.2) can be in one of three states: a steady depolarized state, a bursting state, or a spiking state. We now use our analysis from section 4.1 to construct singular approximations of (2.2) in order to understand the transient and long-term evolution for each of the three attractors. For convenience, we introduce some notation. We denote solutions of the fully perturbed problem (2.2) by $\Gamma_{(\varepsilon,\delta)}$. We write $\Gamma^x_{(0,\delta)}, x \in \{F, I\}$ to denote trajectories of the fast subsystem (4.1) and "slow" subsystem (4.2) written over the intermediate timescale t_I. The singular orbits we construct take the form

$$\Gamma^F_{(0,\delta)} \cup \Gamma^I_{(0,\delta)},$$

where $\Gamma^F_{(0,\delta)}$ represents fast jumps in V and $\Gamma^I_{(0,\delta)}$ is the "slow" flow along S.

Figure 5 illustrates the 1-fast/3-slow singular orbit construction for equilibria and periodic orbits. In each case, the folded singularities M_δ (red), c-nullcline (dashed, black) and full system trajectory $\Gamma_{(\varepsilon,\delta)}$ (black) are plotted. When the attractor of the system is a depolarized steady state (panels (a) and (b)), the singular trajectory is simple, consisting of a fast and a "slow" orbit segment. The fast evolution $\Gamma^F_{(0,\delta)}$ brings the trajectory onto an attracting sheet of the critical manifold S. On S, the layer flow predicts trivial dynamics. The appropriate approximation, then, is the reduced system (4.6), which prescribes a nontrivial flow on S. We observe that the "slow" orbit segment $\Gamma^I_{(0,\delta)}$ converges to the equilibrium point E. The full system trajectory $\Gamma_{(\varepsilon,\delta)}$ then shows that the singular orbit is a suitable predictor of the transient evolution to the equilibrium. More precisely, since the singular trajectories stay in normally hyperbolic regions of S, the full system trajectory $\Gamma_{(\varepsilon,\delta)}$ is simply an $\mathcal{O}(\varepsilon)$ perturbation of the singular attractor $\Gamma^F_{(0,\delta)} \cup \Gamma^I_{(0,\delta)}$ (by Fenichel theory).

Parameter variations shift the position of the steady state on S. There eventually comes a point when the equilibrium crosses the fold surface L and moves from an attracting sheet S^a to a repelling sheet S^r. When the equilibrium crosses the fold surface L, we observe a transcritical bifurcation of an ordinary singularity with a folded singularity. Thus, we have an FSN II bifurcation leading to the birth of limit cycles [20]. Figures 5(c) and (d) show that the 1-fast/3-slow singular attractor is composed of a fast jump from a folded node together with a "slow" flow that returns the orbit to the folded node. That is, we have the singular limit representation of a canard-induced (dynamic) MMO [9].

Fortunately, the main results of canard theory in the case of two slow variables (see section 6.4) carry over to the case of k slow variables, where $k \geq 2$ [63]. Thus, we can supplement our understanding by using a well-known result from the 2-timescale theory. Namely, the maximal number of small amplitude oscillations, $s_{\max}$, of an MMO of the full system can be bounded for sufficiently small perturbations [49, 62, 9]. This bound $s_{\max}$ depends on the eigenvalue

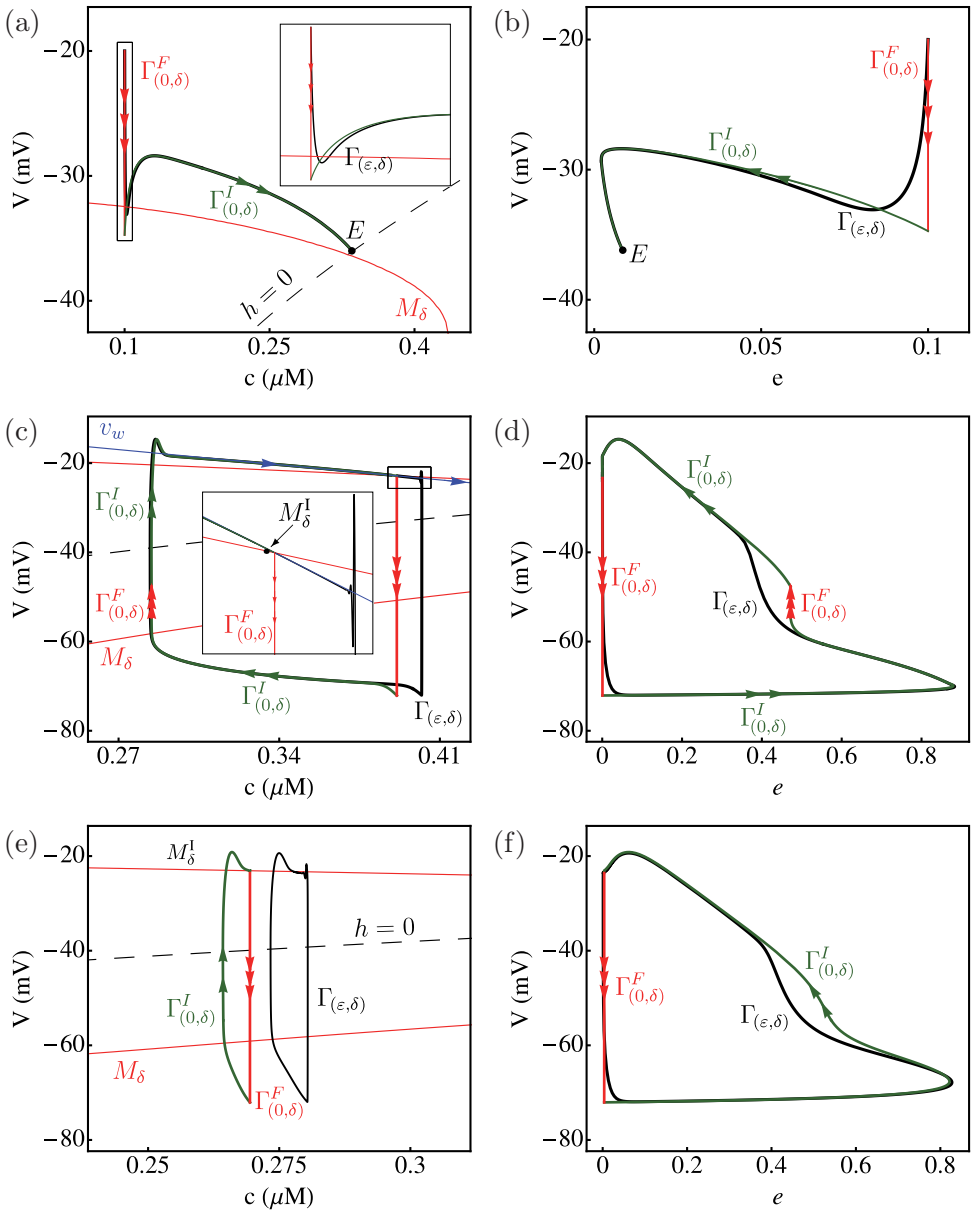

Figure 5. *Singular orbit construction for equilibria (top row) and periodic orbits (middle and bottom rows) projected onto the (V, c) plane (left column) and the (V, e) plane (right column). For* (a) *and* (b), $g_K = 5$ nS, $g_{BK} = 3$ nS, *and* $g_A = 10$ nS. *The full system trajectory has* $C_m = 2$ pF *and* $f_c = 0.01$. *For panels* (c) *and* (d), $g_K = 3$ nS, $g_{BK} = 0.4$ nS, *and* $g_A = 8$ nS. *Panels* (e) *and* (f) *have* $g_K = 5$ nS, $g_{BK} = 0.4$ nS, *and* $g_A = 8$ nS. *The solution of* (2.2) *in panels* (c)–(f) *has* $C_m = 0.2$ pF *and* $f_c = 0.001$.

ratio $\mu = \lambda_w/\lambda_s$ (where $|\lambda_w| < |\lambda_s|$) of the folded node:

$$s_{\max} := \left\lfloor \frac{\mu + 1}{2\mu} \right\rfloor . \tag{4.11}$$

In Figures 5(c) and (d), we find that the folded node of the singular attractor is $\mathcal{O}(\delta)$ close to an FSN I point M_δ^{II}. This means the eigenvalue ratio is $\mu = \mathcal{O}(\delta)$ and $s_{\max}$ is large. However, we typically do not see the maximal number of subthreshold oscillations. Moreover, the small oscillations occur some distance away from the folded node. This can again be accounted for by properties of the folded node. Figure 5(c) shows that the singular MMO approaches the folded node along its weak eigendirection, v_w. The weak eigendirection serves as a linear approximation to the axis of rotation for the small oscillations. Thus, the small oscillations of trajectories close to v_w are not observed until the trajectory is some maximal distance from the folded node and is repelled. In light of this canard theory, we can easily see that the offset between singular and nonsingular trajectories around the folded node (most prominent in Figure 5(c)) is due to the oscillatory behavior.

Figure 5(d) shows that the folded node is not the only region where there is disparity between $\Gamma_{(\varepsilon,\delta)}$ and its singular counterpart. At the "slow"-fast transition near $e \approx 0.4$, the full system trajectory deviates significantly from the predicted path before it realigns with the "slow" orbit segment. To understand the discrepancy, we must consider the geometry of the critical manifold more carefully. Recall that S is folded with fold surface L. In fact, L itself is folded with a curve, C, of cusp bifurcations, where different branches of L coalesce (not shown). This creates an unusual scenario in a neighborhood of C, where trajectories may either encounter L with ever-shortening fast up-jumps or they may avoid L entirely by circumventing C (as in Figure 5(f)). The scenario depicted in Figure 5(d) shows that the singular orbits are close to the curve of cusps (since $\Gamma^F_{(0,\delta)}$ is so short), and consequently, the full system trajectories exhibit slow passage effects associated with a cusp. Currently, cusp singularities in slow/fast systems have been treated only for the case of a single cusp point [7], whereas our system presents a whole curve of them. Numerically, we observe that small perturbations to C change the geometry of the trajectory significantly (as highlighted by Figures 5(d) and (f)), but the precise details are unknown and left to future work.

In section 2, we distinguished between two types of MMOs: dynamic (where the slow variations in the calcium drive the bursts) and calcium-conducting (where the calcium oscillations follow the burst, rather than drive it). As far as the 1-fast/3-slow decomposition is concerned, there is no intrinsic difference between dynamic MMOs and calcium-conducting MMOs. In both cases, the singular orbit is a concatenation of "slow" and fast segments that join continuously at a folded node. The main observation is that dynamic MMOs have $\mu = \mathcal{O}(\delta)$, while calcium-conducting MMOs have μ above some threshold. Figure 5(e) suggests that the singular orbit is not a very good predictor of the full system calcium-conducting MMO. Figure 5(f) counterbalances this and reveals that the (V, c) projection is a special projection in which the approximation error is most pronounced. As before, $\Gamma_{(\varepsilon,\delta)}$ and $\Gamma^F_{(0,\delta)} \cup \Gamma^I_{(0,\delta)}$ are separated by an $\mathcal{O}(\varepsilon)$ distance except near the folded node and the cusp (which is circumvented in this case).

The other attractor we need to consider in our 1-fast/3-slow analysis is the spiking orbit (not shown). Once again, properties of folded nodes can be used to tell the difference between the spiking attractor and the MMO attractor. The funnel of a folded node is the 2D trapping region of S that filters all solutions into that folded node. It is delimited by the strong canard (the unique trajectory γ_0 tangent to the strong eigendirection) of the folded node and by the fold surface L. Each folded node of M_δ possesses a 2D funnel, and together, these form a

3D funnel volume for M_δ. Singular orbits that land inside the funnel volume on their fast upstroke will jump at one of the folded nodes of M_δ and so correspond to MMOs. Singular orbits that land outside the funnel volume on their fast upstroke will return to L at either a regular jump point or at a folded focus, which has no canards. In that case the singular orbit is a relaxation oscillation and corresponds to spiking trajectories of the full system.

Remark 4.3. Note that the funnel of the folded nodes of M_δ is a theoretical construct that loses practical utility as the number of slow variables increases. The concept is truly effective only in the case of two slow variables where M_δ is a single point, the funnel of M_δ is a 2D region, and everything can be visualized (see section 6.5). In practice, a simpler way of identifying a spiking trajectory is to monitor F_δ and the eigenvalues of (4.6) at the upper jump point of the singular orbit. More precisely, if $F_\delta \neq 0$ at the upper jump point, then the singular orbit hits the fold surface at a regular jump point. Alternatively, if $F_\delta = 0$ but the eigenvalues of (4.6) are complex, then the singular orbit jumps at a folded focus.

We have now computed the main objects essential to a standard 2-timescale geometric singular perturbation analysis. We point out that additional information can be obtained from the singular analysis, but within the scope of this paper, we have extracted the chief ingredients. In the 1-fast/3-slow splitting, the bursting behavior is the result of canard dynamics associated with a folded node singularity [49, 62, 9, 14]. This 1-fast/3-slow decomposition is somewhat new in the sense that only relatively recently has it become an established method in mathematical neuroscience for understanding bursting phenomena. Early work on the analysis of neural bursters used an alternative slow/fast analysis. The next section reviews the main components of this more traditional approach.

5. The δ-viewpoint.

The classic slow/fast analysis, pioneered by [40], treats δ as the principal perturbation parameter. It has been used to great effect in unravelling the dynamics of plateau or square wave bursting in pancreatic islets [5], trigeminal motoneurons [10], and neonatal CA3 hippocampal principal neurons [46]. The classical slow/fast splitting is also useful in explaining how pseudo-plateau bursting can be converted to plateau bursting [54]. Here, we review the classic approach and apply it to our system (2.2). In this particular viewpoint, the system is partitioned such that c is the sole slow variable and everything else is relatively fast [4, 32, 38]. In the language of geometric singular perturbation theory, (2.2) is a singularly perturbed problem with small perturbation parameter δ and fixed nonzero ε.

5.1. Geometric singular perturbation analysis.

When using δ as the perturbation parameter, system (2.2) can be considered to have three fast variables (V, n, e) and one slow variable c. In this 3-fast/1-slow analysis, the equivalent "fast" and slow systems are given by (2.2) (or (2.3)) and (2.4), respectively. The singular limit $\delta \to 0$ in (2.2) gives the 3D layer problem

$$\begin{aligned} \varepsilon \frac{dV}{dt_I} &= f(V, n, e, c), \\ \frac{dn}{dt_I} &= g_1(V, n), \\ \frac{de}{dt_I} &= g_2(V, e), \end{aligned} \tag{5.1}$$

$$\frac{dc}{dt_I} = 0,$$

in which the slow variable c is assumed to be so slow that it is essentially fixed. Another approximation of (2.2) assumes the "fast" processes are extremely rapid compared with the c dynamics. By taking the singular limit $\delta \to 0$ in (2.4), i.e., on the slow timescale t_S, we have the 1D reduced problem

$$\begin{aligned} 0 &= f(V,n,e,c), \\ 0 &= g_1(V,n), \\ 0 &= g_2(V,e), \\ \frac{dc}{dt_S} &= h(V,c), \end{aligned} \tag{5.2}$$

where (V,n,e) adjust instantaneously to changes in the slow variable c.

Remark 5.1. Obviously, the layer problem (5.1) of the 3-fast/1-slow method is another singularly perturbed problem with small parameter ε. In fact, it is precisely the 3D model reduction of (2.2) dealt with in [55] and subsequent studies. Our objective here is to illustrate the strengths and weaknesses of the 2-timescale method with perturbation parameter δ. As such, we defer discussion of the full 3-timescale structure to section 6.

To understand the dynamics of the simpler subsystems (5.1) and (5.2), we proceed with a bifurcation analysis, as usual. The critical manifold of the 3D layer problem is the set of equilibria of (5.1), defined by

$$\mathcal{Z} := \left\{(V,n,e,c) \in \mathbb{R}^4 : f(V,n,e,c) = g_1(V,n) = g_2(V,e) = 0\right\}, \tag{5.3}$$

which is a 1D subset of the critical manifold S. Often, we deal with critical manifolds $\mathcal{Z}$ which are folded curves with isolated fold points $\mathcal{L}$ defined by

$$\mathcal{L} := \left\{ (V,n,e,c) \in \mathcal{Z} : \det \begin{pmatrix} f_V & f_n & f_e \\ g_{1V} & g_{1n} & 0 \\ g_{2V} & 0 & g_{2e} \end{pmatrix} = 0 \right\}. \tag{5.4}$$

In the classic slow/fast analysis, $\mathcal{Z}$ is known as the "z-curve" and the fold points $\mathcal{L}$ are called the "knees." The other generic codimension one bifurcation we may encounter is the Andronov–Hopf bifurcation. A standard analysis of the eigenvalues of (5.1) shows that the Hopf bifurcation is given by the condition

$$\mathcal{Z}^H := \left\{(V,n,e,c) \in \mathcal{Z} : f_V = \varepsilon\, H(V,n,e,c,\varepsilon)\right\}, \tag{5.5}$$

where $H(V,n,e,c,\varepsilon)$ can be computed explicitly. Note that there are other Hopf bifurcations on $\mathcal{Z}$, but these have been found (numerically) to occur on the repelling branch $\mathcal{Z}^r$ of $\mathcal{Z}$, and so we will concentrate only on those Hopfs that are $\mathcal{O}(\varepsilon)$ close to the fold surface L. The criticality of the fast subsystem Hopf typically differentiates between plateau and pseudo-plateau bursting [47, 39, 56, 54]. In our model system, $\mathcal{Z}^H$ has always been found (numerically) to be subcritical so that the associated bursts are of pseudo-plateau type.

System (5.2) describes the slow motions on the restricted phase space $\mathcal{Z}$. A complete description of (5.2) is obtained by projection:

$$\frac{d}{dt_S}\begin{pmatrix} V \\ n \\ e \end{pmatrix} = -\begin{pmatrix} f_V & f_n & f_e \\ g_{1V} & g_{1n} & 0 \\ g_{2V} & 0 & g_{2e} \end{pmatrix}^{-1}\begin{pmatrix} f_c h \\ 0 \\ 0 \end{pmatrix} = \frac{1}{\det A}\begin{pmatrix} -g_{1n}g_{2e} \\ g_{1V}g_{2e} \\ g_{1n}g_{2V} \end{pmatrix} f_c h, \tag{5.6}$$

where A is the matrix appearing in (5.4). We note that the slow flow along $\mathcal{Z}$ is singular at the folds $\mathscr{L}$. For our model, the only singularities of the slow subsystem are the equilibria E of the fully perturbed problem. However, it is conceivable that there are discrete parameter values, g_* say, where the full system equilibrium coincides with a fold point $\mathscr{L}$ and a singular Hopf bifurcation may occur [39]. That is, it is possible that the set

$$\mathscr{L} \cap E = \{(V, n, e, c) \in \mathscr{L} : h(V, c) = 0\}$$

is nonempty and a canard point of (5.6) exists, making canard solutions feasible in an exponentially small parameter window localized around g_*. Despite this, such canard points have no bearing on the full system dynamics since they have always been found (numerically) to occur on the repelling branch of $\mathcal{Z}$. This is due to the geometric structure of $\mathcal{Z}$ wherein the Hopf point $\mathcal{Z}^H$ occurs at a more depolarized voltage level than the fold points $\mathscr{L}$. Consequently, any canard points must occur on $\mathcal{Z}^r$ and the singular attractor of (5.1) and (5.2) never visits the canard point. As such, (2.2) has no (observable) canard dynamics with respect to the slow-fast decomposition (5.1)–(5.2) and the oscillatory behavior cannot be due to a folded node. The oscillation mechanism must be encoded, then, in the layer problem (5.1).

5.2. Singular orbits and bifurcations. We can now proceed to construct singular orbits as in the previous section to extract useful information about the dynamics. The singular orbits

$$\Gamma^I_{(\varepsilon,0)} \cup \Gamma^S_{(\varepsilon,0)}$$

are continuous concatenations of solutions of (5.1) and (5.2), denoted by $\Gamma^I_{(\varepsilon,0)}$ and $\Gamma^S_{(\varepsilon,0)}$, respectively. Figure 6 shows the 3-fast/1-slow singular orbit construction for equilibria and for dynamic MMOs.

In Figures 6(a) and (b), the equilibrium E of (2.2) sits on $\mathcal{Z}^a$. Initial conditions generically start away from $\mathcal{Z}$, and so the first part of the transient evolution is a rapid motion $\Gamma^I_{(\varepsilon,0)}$ towards the critical manifold $\mathcal{Z}$. Due to the slow/fast structure of (5.1), the "fast" orbit segment initially overshoots $\mathcal{Z}$ before settling down to it. The slow flow $\Gamma^S_{(\varepsilon,0)}$ along $\mathcal{Z}^a$ brings the trajectory to E before it can reach either the Hopf point $\mathcal{Z}^H$ or the fold point $\mathscr{L}$. Since the singular orbit stays away from bifurcations of the "fast" and slow subsystems, Fenichel theory guarantees that the full system trajectory $\Gamma_{(\varepsilon,\delta)}$ is an $\mathcal{O}(\delta)$ perturbation of $\Gamma^I_{(\varepsilon,0)} \cup \Gamma^S_{(\varepsilon,0)}$. Note that the asymptotic matching in this case occurs at $\mathcal{Z}$, where the reduced problem (outer solution) and layer problem (inner solution) overlap (cf. Figures 5(a) and (b)).

Parameter variations move E through $\mathcal{Z}^H$, and the attractor eventually becomes a limit cycle. The singular dynamic MMO attractor is a hysteresis loop that alternates between the attracting branches of $\mathcal{Z}$ (Figures 6(c) and (d)). The singular orbit jumps at the fold point

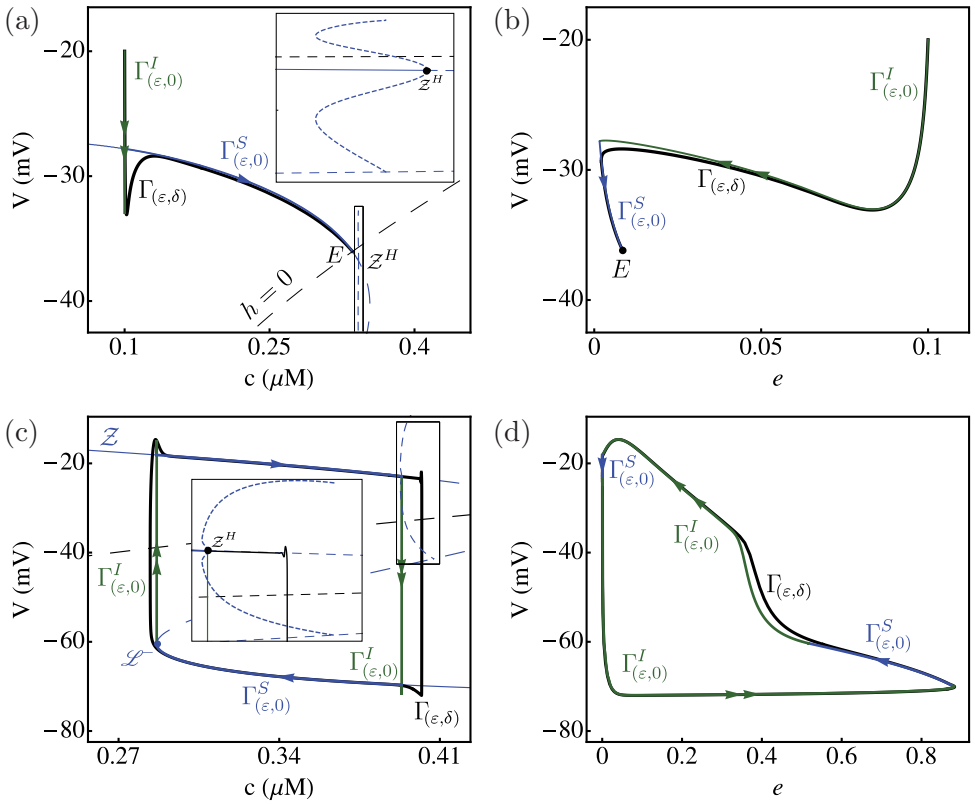

Figure 6. *Singular orbit and one-parameter bifurcation diagram (with bifurcation parameter c) for equilibria (top row) and dynamic MMOs (bottom row). Parameter values in* (a) *and* (b) *are* $g_K = 5$ nS, $g_{BK} = 3$ nS, *and* $g_A = 10$ nS *with* $C_m = 2$ pF *and* $f_c = 0.01$ *for* $\Gamma_{(\varepsilon,\delta)}$ *(cf. Figures* 5(a) *and* (b)*). In* (c) *and* (d), $g_K = 3$ nS, $g_{BK} = 0.4$ nS, *and* $g_A = 8$ nS *with* $C_m = 0.2$ pF *and* $f_c = 0.001$ *for* $\Gamma_{(\varepsilon,\delta)}$ *(cf. Figures* 5(c) *and* (d)*). In both cases, there is an unstable spiking branch (blue, dashed) emanating from the subcritical Hopf bifurcation of* (5.1).

$\mathcal{L}^-$ and also at the (subcritical) Hopf bifurcation $\mathcal{Z}^H$. The inset of Figure 6(c) shows that the full system trajectory $\Gamma_{(\varepsilon,\delta)}$ does not immediately jump when it passes through $\mathcal{Z}^H$. Instead, there is a long delay in which the trajectory traces out $\mathcal{Z}^r$ before it eventually displays small amplitude oscillations and jumps to a different branch of $\mathcal{Z}$. Thus, we have a Hopf bifurcation of the layer problem (5.1) that is unrelated to equilibria of the full system (2.2), which causes delayed oscillations. Hence, according to the 3-fast/1-slow analysis, the oscillation mechanism of dynamic MMOs is a delayed Hopf bifurcation [3, 14, 21].

The flow of (2.2) in a neighborhood of $\mathcal{Z}^H$ can be understood in very simple terms. For $\delta = 0$, the variable c is a fixed parameter, but for $0 < \delta \ll 1$, c is a slow variable that drifts through the vicinity of the Hopf bifurcation. Near the Hopf, we can write

$$\mathcal{Z} = \mathcal{Z}^a \cup \mathcal{Z}^H \cup \mathcal{Z}^r,$$

where $\mathcal{Z}^a$ and $\mathcal{Z}^r$ denote the parts of $\mathcal{Z}$ with eigenvalues having negative and positive real parts, respectively. Trajectories that approach $\mathcal{Z}^a$ a distance $\mathcal{O}(1)$ from the Hopf bifurcation

are attracted to and oscillate around $\mathcal{Z}^a$. Exponential contraction of the system means that the trajectory becomes exponentially close to $\mathcal{Z}^a$ on the slow timescale as it passes close to $\mathcal{Z}^H$. As the trajectories pass over to $\mathcal{Z}^r$, the layer equations undergo a Hopf bifurcation, but in analytic systems, the trajectories remain close to $\mathcal{Z}^r$ for $\mathcal{O}(1)$ times. That is, trajectories remain close to $\mathcal{Z}^r$ for an $\mathcal{O}(1)$ distance after the Hopf bifurcation $\mathcal{Z}^H$ has occurred. The delay occurs because the trajectory is exponentially close to $\mathcal{Z}$ and must be repelled before it can follow limit cycles of the layer problem. Furthermore, the slow/fast analysis can identify buffer points, which determine the maximal distance orbits can trace $\mathcal{Z}^r$ before they must leave $\mathcal{Z}^r$ and oscillate [36, 37, 3]. Typically, the small amplitude oscillations associated with the passage through the Hopf are below a visible threshold, resulting in trajectories that are virtually indistinguishable from the manifold $\mathcal{Z}$.

Remark 5.2. Apart from the fast subsystem Hopf point, the other bifurcation point in the singular orbit is the fold point $\mathscr{L}^-$. The behavior of the full system trajectory $\Gamma_{(\varepsilon,\delta)}$ in a neighborhood of $\mathscr{L}^-$ is that of classic fold behavior [30, 50]. More specifically, consider a section perpendicular to the fast direction at $V = -40$, say. The full system trajectory $\Gamma_{(\varepsilon,\delta)}$ and the layer solution that jumps from $\mathscr{L}^-$ pass through this section $\mathcal{O}(\delta^{2/3})$ close to each other. At an $\mathcal{O}(1)$ distance from the singular points $\mathcal{Z}^H$ and $\mathscr{L}^-$, the full system trajectory is $\mathcal{O}(\delta)$ close to $\Gamma^I_{(\varepsilon,0)} \cup \Gamma^S_{(\varepsilon,0)}$.

5.3. The distinction between MMO types. As noted in Figure 6(c), the singular dynamic MMO orbit is a hysteresis cycle that jumps at the thresholds $\mathscr{L}^-$ and $\mathcal{Z}^H$, where $\mathscr{L}^-$ sits to the left of $\mathcal{Z}^H$ in the (V, c) projection. Under variation of the conductances (g_K, g_{BK}, g_A), the positions of the fold point $\mathscr{L}^-$ and the Hopf point $\mathcal{Z}^H$ change. We immediately see an issue: what happens when $\mathscr{L}^-$ sits to the right of $\mathcal{Z}^H$ so that the bistable region of $\mathcal{Z}$ disappears? We illustrate the problem in Figure 7.

Figure 7 is a prototypical example of a scenario in which the fold point $\mathscr{L}^-$ sits to the right of the Hopf point $\mathcal{Z}^H$. The attractor $\Gamma_{(\varepsilon,\delta)}$ of the fully perturbed problem (2.2) sits in the c-interval between the two bifurcation points. Transients of the fully perturbed problem closely trace the critical manifold $\mathcal{Z}$ until they encounter either $\mathscr{L}^-$ or $\mathcal{Z}^H$, at which point they start bursting (Figure 7(a)). The transient bursting exhibits differing numbers of small amplitude oscillations, depending on the position of the trajectory in phase space. An explanation of this dynamical behavior using geometric singular perturbation theory requires more work than in previous scenarios.

For our transient singular orbit construction we can, without loss of generality, take an initial condition on the curve $\mathcal{Z}^a$. Transients move along $\mathcal{Z}^a$ (described by the reduced problem (5.2)) until they encounter the fold point $\mathscr{L}^-$ or the Hopf point $\mathcal{Z}^H$ (where normal hyperbolicity breaks down). At the fold point $\mathscr{L}^-$, the layer flow description (5.1) takes over and it generates a stable MMO, $\Gamma^1_{(\varepsilon,0)}$, with fixed c. Similarly, at $\mathcal{Z}^H$ the layer problem, (5.1) produces a stable MMO, $\Gamma^2_{(\varepsilon,0)}$, with c fixed at $\mathcal{Z}^H$ (Figures 7(b) and (c)). We then find that for every fixed c value between $\mathcal{Z}^H$ and $\mathscr{L}^-$, the attractor of (5.1) is an MMO (not shown). In short, when there is no bistability in $\mathcal{Z}$, the 3-fast/1-slow splitting predicts a torus of MMOs of calcium-conducting type between $\mathcal{Z}^H$ and $\mathscr{L}^-$.

Remark 5.3. Recall from section 4.2 that there is a curve of cusp bifurcations in the 1-fast/3-slow splitting, where the trajectories deviate significantly from the singular limit

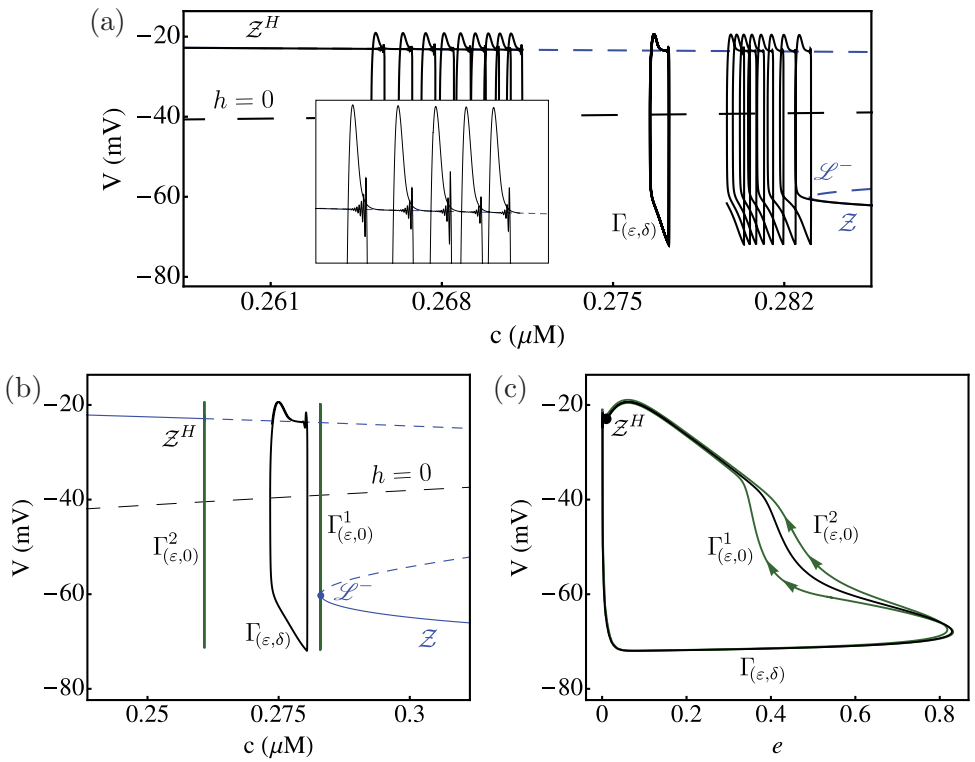

Figure 7. *Geometric configuration of $\mathcal{Z}$ in which there is no bistability for $g_K = 5$ nS, $g_{BK} = 0.4$ nS, and $g_A = 8$ nS (cf. Figures 5(e) and (f)). In* (a) *the transient evolution to the attractor of (2.2) with $C_m = 0.2$ pF, $f_c = 0.0001$ exhibits a variety of bursts. In* (b) *there is a c-interval of stable singular MMOs bounded by $\Gamma^1_{(0,0)}$ and $\Gamma^2_{(0,0)}$ (see text). The attractor of the fully perturbed problem $\Gamma_{(\varepsilon,\delta)}$ for $C_m = 0.2$ pF, $f_c = 0.001$ lies somewhere in this c-interval.* (c) *The (V, e) projection shows a clearer picture of the periodic orbits.*

predictions. Figure 7(c) shows that the cusp continues to play a role in shaping the trajectories. However, in the 3-fast/1-slow setting, the cusp cannot be detected, and hence the disparity between singular and nonsingular orbits cannot be explained.

Within this torus of stable singular MMOs, there is a unique singular attractor that the full system attractor $\Gamma_{(\varepsilon,\delta)}$ converges to in the singular limit $\delta \to 0$. To locate this singular attractor, we use averaging. A rigorous discussion of the averaging method is presented in [45], and we also refer the reader to [4, 6] for examples of the method applied to singular perturbation problems. In the context of our lactotroph model (2.2), the autonomous averaged equation (to leading order) for the slow motions is

$$\frac{dc}{dt_I} = \delta \frac{1}{T(c)} \int_0^{T(c)} h(V_{(\varepsilon,0)}(s,c),c)\, ds \equiv \delta \overline{h}(c), \tag{5.7}$$

where $V_{(\varepsilon,0)}(t,c)$ is the V-coordinate of the MMO attractor of (5.1) with period $T(c)$ for a fixed c between $\mathcal{Z}^H$ and $\mathcal{L}^-$. We are interested in equilibria of (5.7), where there is no net drift in c.

Figure 8 shows how the averaging method can be used to approximate the MMO attractor of (2.2). In panel (a), the averaged vector field $\overline{h}(c)$ is plotted over the c-interval between

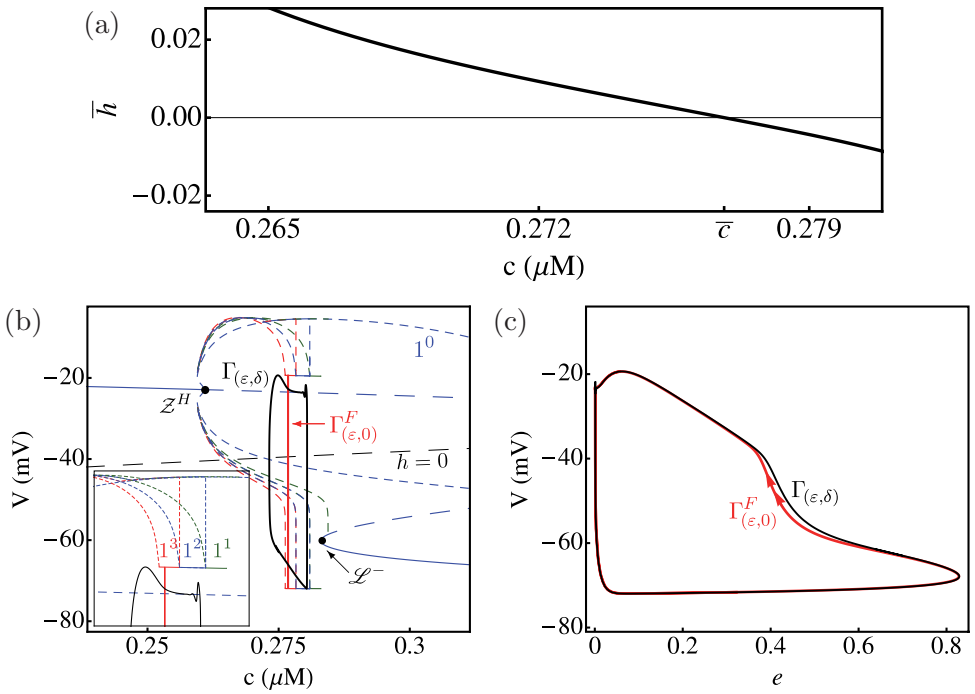

Figure 8. *The averaging method for the parameter set given in Figure 7.* (a) *The function* $\overline{h}(c)$ *plotted over the c-interval between* $\mathcal{Z}^H$ *and* $\mathcal{L}^-$ *shows that* (5.7) *has a unique stable equilibrium.* (b) *Bifurcation structure of the layer problem* (5.1). *The maxima and minima of the various MMO families are shown. The spiking family comes from the Hopf* $\mathcal{Z}^H$, *and the MMO families with* $s \geq 1$ *are born nearby.* (c) *The singular averaged MMO attractor (red,* $\Gamma^F_{(\varepsilon,0)}$*) is a good approximation of the full system trajectory* $\Gamma_{(\varepsilon,\delta)}$.

$\mathcal{Z}^H$ and $\mathcal{L}^-$. We can immediately see that the averaged equation (5.7) has a single stable equilibrium at $\overline{c} \approx 0.277$ μM. We then use $\overline{c}$ in the layer problem (5.1) to generate a stable singular MMO. Panel (b) shows the bifurcation structure of (5.1) with respect to c. The critical manifold $\mathcal{Z}$ is unstable over the c-interval between the Hopf bifurcation $\mathcal{Z}^H$ and the lower fold point $\mathcal{L}^-$. Emanating from the Hopf point is the unstable spiking branch (labeled 1^0), which terminates in homoclinic points on the unstable branch of $\mathcal{Z}$. There exist stable MMO families in the c-interval between $\mathcal{Z}^H$ and $\mathcal{L}^-$. These are computed in AUTO using c as the principal continuation parameter.

In Figure 8, the MMO family for $s = 1$ (green) has a small window of stability and terminates at homoclinics. The adjacent MMO branch for $s = 2$ (blue) is a closed isola of orbits. Similarly, the $s = 3$ branch (red) is an isola of MMOs with a stability window adjacent to the stability window of the $s = 2$ branch. Further calculations show that there are additional MMO families within the c-interval between the Hopf $\mathcal{Z}^H$ and the fold point $\mathcal{L}^-$. The number of subthreshold oscillations s increases as c tends towards $\mathcal{Z}^H$. The singular averaged attractor, $\Gamma^F_{(\varepsilon,0)}$, is then superimposed on the bifurcation diagram in Figure 8. We observe that $\Gamma^F_{(\varepsilon,0)}$ lies in the stable window of the 1^3 MMOs and that $\Gamma_{(\varepsilon,\delta)}$ itself is a 1^3 MMO. Moreover, since the singular orbit $\Gamma^F_{(\varepsilon,0)}$ with $c = \overline{c}$ never runs into any singularities, Fenichel theory holds and $\Gamma_{(\varepsilon,\delta)}$ is an $\mathcal{O}(\delta)$ perturbation of the averaged singular orbit. In this

way, we can use the singular limit $\delta \to 0$ to predict the full system dynamics.

Variations in the conductances change the bifurcation structure of (5.1). By choosing parameter sets closer to the spiking/bursting boundary (see Figure 4), the MMO families are pushed to lower c values. That is, the MMO branches with large s are squeezed into ever-decreasing neighborhoods of $\mathcal{Z}^H$. The averaged singular MMO moves through these MMO families towards the fold point $\mathscr{L}^-$ and thus traverses the MMOs with smaller s. Eventually, the $s = 0$ branch itself becomes stable and the averaged MMO trajectory lies in the stability plateau of the spiking family.

Thus, the 3-fast/1-slow analysis can be used to explain the main dynamical behaviors of (2.2): depolarized steady states, (dynamic and calcium-conducting) MMOs, and spiking. In particular, the bifurcation structure of $\mathcal{Z}$ provides a simple test for dynamic or calcium-conducting MMOs. A Hopf bifurcation in the layer problem explains the oscillation mechanism of dynamic MMOs. For calcium-conducting MMOs, however, the singular analysis does not provide any clear oscillation mechanism.

6. The 3-timescale problem.

So far we have taken two different approaches to the analysis of the 3-timescale problem (2.2). In the 1-fast/3-slow approach, we found that the MMOs were due to canards, which provided a strong theoretical framework for explaining the delay phenomena. However, the canard theory had no way of distinguishing between dynamic MMOs and calcium-conducting MMOs. Then, in the 3-fast/1-slow approach, we had a very simple criterion to differentiate between the two MMO types based on the geometric configuration of $\mathcal{Z}$, but we did not have a clear oscillation mechanism. In each case, we alluded to the presence of the third timescale (but made no use of it). In this section, we finally acknowledge the full 3-timescale structure of (2.2) and perform a geometric singular perturbation analysis. Analyses of 3-timescale problems are currently rare [25, 28, 29, 52], and a rigorous theoretical framework has yet to be developed. Regardless, we demonstrate that our approach is effective for dealing with 3-timescale problems. In particular, we show that the 3-timescale analysis combines the information from 2-timescale methodologies, affording us greater predictive power than any of the 2-timescale approaches.

6.1. Geometric singular perturbation analysis.

Recall that the lactotroph model (2.2) is a 3-timescale problem with fast variable V, intermediate variables (n, e), and slow variable c. We have observed in the transient evolution of (2.2) that the fastest timescale initially dominates the evolution. The slower timescales come into effect when the trajectory enters some special neighborhood of phase space (either S or $\mathcal{Z}$). With this in mind, we proceed to define the singular subsystems of the 3-timescale problem in the order in which we expect to encounter them.

The double limit $(\varepsilon, \delta) \to (0, 0)$ on the fast timescale gives the *fast subsystem*, which is the approximation of (2.2) in which the intermediate and slow variables (n, e, c) move so slowly (compared to V) that they are fixed. The fast subsystem is precisely the layer problem (4.1) of the 1-fast/3-slow approach. The double limit on the intermediate timescale t_I gives the 2D *intermediate subsystem*

$$0 = f(V, n, e, c), \tag{6.1}$$

$$\frac{dn}{dt_I} = g_1(V,n),$$
$$\frac{de}{dt_I} = g_2(V,e),$$
$$\frac{dc}{dt_I} = 0,$$

an approximation of (2.2) in which V is sufficiently rapid that it immediately responds to changes in state and c is sufficiently slow that it has no movement. Note that (6.1) is the $\delta \to 0$ limit of the 3D reduced problem (4.2) of the 1-fast/3-slow splitting. It is also the $\varepsilon \to 0$ limit of the 3D layer problem (5.1) of the 3-fast/1-slow decomposition. Thus, we can interpret the intermediate subsystem (6.1) as the interaction between the 1-fast/3-slow and 3-fast/1-slow analyses. What that means, as we will show, is that all the geometric structures encountered previously persist in the double limit.

We inherit the 3D critical manifold S (and its 2D fold surface L), which serves as a manifold of equilibria of the fast subsystem and as the phase space of the intermediate subsystem (6.1). Projection and desingularization of (6.1) give a complete description of the nontrivial flow on S:

$$\begin{aligned} \frac{dV}{dt_I^*} &= F_0(V,n,e,c) \equiv f_n\, g_1 + f_e\, g_2, \\ \frac{de}{dt_I^*} &= -f_V\, g_2(V,e), \\ \frac{dc}{dt_I^*} &= 0, \end{aligned} \tag{6.2}$$

where n is determined by (4.3). The desingularized system (6.2) inherits the curve of folded singularities M_0, where M_0 is simply the $\delta \to 0$ limit of M_δ:

$$M_0 := \{(V,n,e,c) \in L : F_0(V,n,e,c) = 0\}. \tag{6.3}$$

The ordinary singularities E of (4.6) do not persist as singularities of (6.2). The $\delta \to 0$ limit frees the system from the constraint $h = 0$, and the $\delta \to 0$ analogue of the ordinary singularities is in fact the critical manifold $\mathcal{Z}$ of the 3-fast/1-slow splitting.

Remark 6.1. The persistence of the curve of folded singularities in the desingularized system (6.2) gives us access to canard theory, which in turn provides an oscillation mechanism for the MMOs. Moreover, the presence of the critical manifold $\mathcal{Z}$ in (6.2) provides the geometric information needed to distinguish between dynamic MMOs and calcium-conducting MMOs.

The critical manifold $\mathcal{Z}$ forms a 1D subset of the critical manifold S. As such, we expect bifurcations of (6.2) at bifurcations of (4.1), i.e., at the fold surface L. This can be easily verified by computing the determinant of the Jacobian of (6.2) evaluated along $\mathcal{Z}$:

$$\det \begin{pmatrix} \partial_V(F_0) & \partial_e(F_0) \\ \partial_V(-f_V g_2) & \partial_e(-f_V g_2) \end{pmatrix}\Bigg|_{\mathcal{Z}} = -f_V f_n\, g_{1V} g_{2e},$$

which has opposite sign to f_V. In particular, along the fold surface L, system (6.2) possesses a zero eigenvalue. Thus, the attracting branch $\mathcal{Z}^a$ of $\mathcal{Z}$ is the subset of $\mathcal{Z}$ embedded in S^a along

which the eigenvalues have negative real part. The repelling branch $\mathcal{Z}^r$ of $\mathcal{Z}$ is the subset of $\mathcal{Z}$ (embedded in either S^a or S^r) along which at least one eigenvalue has positive real part.[3]

The curve of folded singularities M_0 consists of folded nodes, saddles, and foci. The folded SN points can be located by examining the Jacobian determinant of (6.2) evaluated along M_0:

$$\det \begin{pmatrix} \partial_V(F_0) & \partial_e(F_0) \\ \partial_V(-f_V g_2) & \partial_e(-f_V g_2) \end{pmatrix}\Big|_{M_0} = g_2 \left(F_{0e} f_{VV} - F_{0V} f_{Ve}\right).$$

It is clear that there are two ways in which an FSN of type I may occur: either $F_{0e} f_{VV} - F_{0V} f_{Ve} = 0$ or $g_2 = 0$. The first case corresponds to actual folds in M_0. In the case $g_2 = 0$, the condition $F_0 = 0$ simplifies to $g_1 = 0$, and thus the corresponding FSN I points are defined by

$$M_0^{\mathrm{I}} := M_0 \cap \mathcal{Z} = \{(V, n, e, c) \in \mathcal{Z} : f_V(V, n, e, c) = 0\}. \tag{6.4}$$

Geometrically, the set M_0^{I} has two interpretations. First, the FSN I points M_0^{I} represent direct interactions between geometric structures of the 1-fast/3-slow (M_0) and 3-fast/1-slow ($\mathcal{Z}$) analyses, respectively. Second, the FSN I points M_0^{I} correspond to crossings of the critical manifold $\mathcal{Z}$ over the fold surface L.

Remark 6.2. With the interpretation of M_0^{I} as crossings of $\mathcal{Z}$ over L in mind, the geometric meaning of (4.10) is now clear. The curve defined by

$$\mathcal{Z}_\delta := \{(V, n, e, c) \in S : g_1 = \delta G_1, g_2 = \delta G_2\}$$

is an $\mathcal{O}(\delta)$ perturbation of the critical manifold $\mathcal{Z}$.

We note that the points of M_0^{I} are the $\varepsilon \to 0$ limit of the Hopf bifurcation points $\mathcal{Z}^H$, defined by (5.5) encountered in the 3-fast/1-slow layer problem. Moreover, M_0^{I} is the $\delta \to 0$ counterpart of the FSN I points M_δ^{I}, defined by (4.10), in the 1-fast/3-slow splitting (cf. [52]). We further note that, as far as (6.2) is concerned, the FSN II points (4.9) are codimension 2 bifurcations (in fact, they are special cases of FSN I points M_0^{I}).

The *slow subsystem* approximation of (2.2) assumes that (V, n, e) are so rapid when compared with c that they immediately settle down to their steady state under changes in c. The slow subsystem is obtained from the double limit $(\varepsilon, \delta) \to (0, 0)$ of the slow system (2.4) and is identical to (5.2). As before, the critical manifold $\mathcal{Z}$ is both the manifold of equilibria of (6.2) and the phase space of the slow subsystem, and the fold points $\mathscr{L}$ are singular points in the slow flow (but they are not singular points of the intermediate flow (6.1)). The only equilibria of (5.2) are the true equilibria E of (2.2).

6.2. Transients and the depolarized steady state. As before, we use our geometric singular perturbation analysis to unravel the dynamics of (2.2). We now write $\Gamma^x_{(0,0)}$, $x \in \{F, I, S\}$, to denote solutions of the fast, intermediate, and slow subsystems (4.1), (6.1), and (5.2), respectively. Our singular orbits take the form

$$\Gamma^F_{(0,0)} \cup \Gamma^I_{(0,0)} \cup \Gamma^S_{(0,0)}.$$

As usual, solutions of the fully perturbed problem are denoted by $\Gamma_{(\varepsilon,\delta)}$.

[3] In principle, we should also consider Hopf bifurcations along $\mathcal{Z}$. Fortuitously, numerical studies show that within the physiological domain, Hopf bifurcations of (6.2) usually occur on the repelling sheet $\mathcal{Z}^r$.

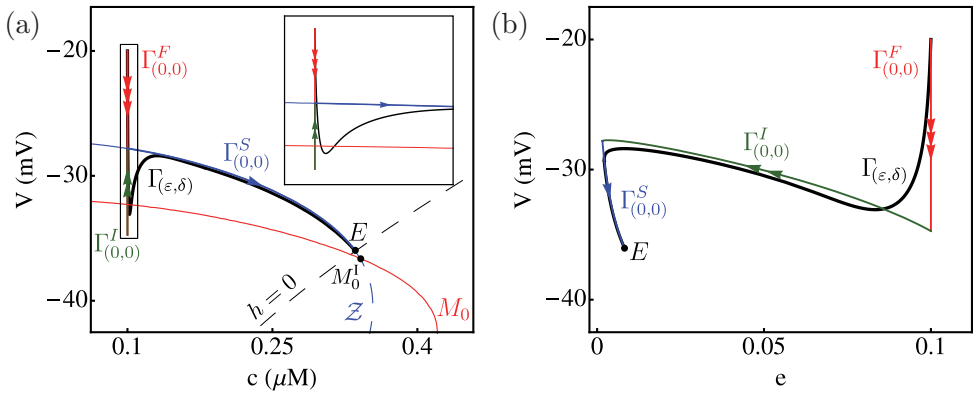

Figure 9. *Singular orbit construction in the case of a stable equilibrium projected onto the* (a) (V,c) *plane or* (b) (V,e) *plane. The parameters are* $g_K = 5$ nS, $g_{BK} = 3$ nS, *and* $g_A = 10$ nS *(cf. Figures 5 and 6, panels* (a) *and* (b)*). The solution* $\Gamma_{(\varepsilon,\delta)}$ *of (2.2) with* $C_m = 2$ pF *and* $f_c = 0.01$ *is approximated by solutions of the fast subsystem (red,* $\Gamma^F_{(0,0)}$*), intermediate subsystem (green,* $\Gamma^I_{(0,0)}$*), and slow subsystem (blue,* $\Gamma^S_{(0,0)}$*). The critical manifold* $\mathcal{Z}$ *(blue) and folded singularities* M_0 *(red) are also shown.*

Figure 9 shows the singular orbit construction in the case when system (2.2) has a stable depolarized steady state. We first identify the main objects from our geometric singular perturbation analysis: the critical manifold $\mathcal{Z}$ intersects the curve of folded singularities M_0 at the FSN I point M_0^{I}. This marks the switch from an attracting branch to a repelling branch (of both S and $\mathcal{Z}$). Both $\mathcal{Z}$ and M_0 are folded. The fold point $\mathscr{L}$ in $\mathcal{Z}$ (not labeled) at $c \approx 0.355$ μM occurs when an eigenvalue changes sign, so that there is a saddle on one side and an unstable node on the other. The fold in M_0 (also not labeled) at $c \approx 0.421$ μM is another FSN I point. The intersection of the critical manifold $\mathcal{Z}$ with the c-nullcline corresponds to a true equilibrium E of (2.2). In Figure 9, E lies on the attracting sheets S^a and $\mathcal{Z}^a$ and so is a stable equilibrium of the full system for sufficiently small perturbations.

We now explain, using our singular limit subsystems, the transient evolution to the attractor starting from arbitrary initial conditions. Since an initial condition is (generically) off the critical manifold S, the fast dynamics (4.1) dominate and there is a rapid evolution $\Gamma^F_{(0,0)}$ along a 1D fast fiber to an attracting branch of S (red, 3 arrows). This is succeeded by an intermediate decay $\Gamma^I_{(0,0)}$ (green, 2 arrows) towards the critical manifold $\mathcal{Z}$. For the example illustrated in Figure 9, the intermediate flow $\Gamma^I_{(0,0)}$ explains the overshoot previously seen in Figure 6(a). Once the trajectory is on $\mathcal{Z}$, the slow flow description (5.2) takes over and the slow drift $\Gamma^S_{(0,0)}$ either brings the orbit towards the depolarized equilibrium state E (blue, 1 arrow) or to the lower fold point $\mathscr{L}^-$, depending on the initial conditions. In the case of the fold point, the intermediate and fast subsystems describe the return of the trajectory to the upper attracting branch of $\mathcal{Z}$ where the slow flow once again brings the trajectory to E.

Remark 6.3. Even though the fold point $\mathscr{L}^-$ is embedded in the critical manifold S, the results from classic studies of fold points hold [35, 50, 58, 63]. This can be shown formally by computing a normal form for $\mathscr{L}^-$, which is beyond the scope of this work. The main result in the context of our 4D 3-timescale problem is that there is a 2D slow/intermediate subsystem that is precisely the classic fold problem and the remaining intermediate and fast directions

are hyperbolic.

Since the singular orbit in Figure 9 does not involve any bifurcations of the fast, intermediate, or slow subsystems, the full system trajectory is an $\mathcal{O}(\varepsilon, \delta)$ perturbation of the singular attractor. Bearing in mind the results of sections 4.2 and 5.2, we can actually make more precise asymptotic statements. At the interface where $\Gamma^F_{(0,0)}$ and $\Gamma^I_{(0,0)}$ meet, the fast timescale switches to the intermediate timescale and the dominant perturbation parameter is ε. This ε-dominance manifests as a nonuniform sensitivity of the trajectories to perturbations in ε and δ in a neighborhood of the timescale switch. That is, small changes in δ have virtually no effect on $\Gamma_{(\varepsilon,\delta)}$ near the fast-intermediate timescale transition, while small changes in ε quickly move $\Gamma_{(\varepsilon,\delta)}$ away from the singular limit prediction. Similarly, the intermediate-slow timescale switch (where $\Gamma^I_{(0,0)}$ and $\Gamma^S_{(0,0)}$ meet) is dominated by δ. Small changes in ε have very minor impact on the full system trajectory near the intermediate-slow transition, whereas small changes in δ cause more substantial deviations.

6.3. Bursting with dynamic calcium. Recall from sections 4 and 5 that the transition from stable depolarized steady states, E, to MMOs occurred when the equilibrium crossed from a stable branch of the critical manifold to an unstable one. The transition occurred via either an FSN II (as in the 1-fast/3-slow case) or via a Hopf bifurcation $\mathcal{Z}^H$ (as in the 3-fast/1-slow case). In the double limit, $\mathcal{Z}^H$ moves to the fold surface L, becoming an FSN I M_0^{I} in the process. Thus, when E crosses from S^a to S^r, it also crosses from $\mathcal{Z}^a$ to $\mathcal{Z}^r$ at the same time. Hence, the switch from depolarized steady states to MMOs still occurs via an FSN II.

As we saw in section 6.2, any transient flow towards $\mathcal{Z}$ can be explained using the fast and intermediate subsystems. We now focus on the singular MMO attractor and examine its key features (Figure 10). The singular MMO consists of seven distinct orbit segments. Starting at the lower fold point $\mathscr{L}^-$, the intermediate flow (6.1) brings the trajectory to the fold surface L. From there, the flow along the fast fibers projects the trajectory onto a different attracting manifold S^a. The intermediate timescale then dominates, and the trajectory is brought into $\mathcal{Z}^a$ (along the weak eigendirection of one of the nodes of $\mathcal{Z}$). The trajectory then travels along $\mathcal{Z}^a$ according to the slow flow (5.2) until it hits the FSN I point M_0^{I}. From M_0^{I}, the trajectory jumps off S^a to an alternate attracting branch of S. Yet another intermediate flow returns the orbit to $\mathcal{Z}$ (again, via the weak eigendirection of a node of $\mathcal{Z}$). The slow subsystem then describes the motion of the trajectory until it returns to the fold point $\mathscr{L}^-$, thus completing the singular MMO attractor. The full system attractor, $\Gamma_{(\varepsilon,\delta)}$, is a perturbation of this singular orbit.

Within our singular MMO attractor, there are three special regions where normal hyperbolicity breaks down. The first is the fold point $\mathscr{L}^-$, which exhibits classic fold behavior [30]. This is where the trajectory transitions from the slow timescale to the intermediate timescale and δ is the important perturbation parameter. Trajectories $\Gamma_{(\varepsilon,\delta)}$ are $\mathcal{O}(\delta^{2/3})$ perturbations of the singular orbit in a neighborhood of $\mathscr{L}^-$. The second nonhyperbolic region encountered is the fold surface L, where the intermediate-fast timescale switch occurs and ε is the important perturbation parameter. This is a well-studied degeneracy in 2-timescale singularly perturbed problems [50]. In our case, however, the fast up-jump is close to a cusp bifurcation (see section 4.2) and the full system trajectory deviates significantly from the singular orbit

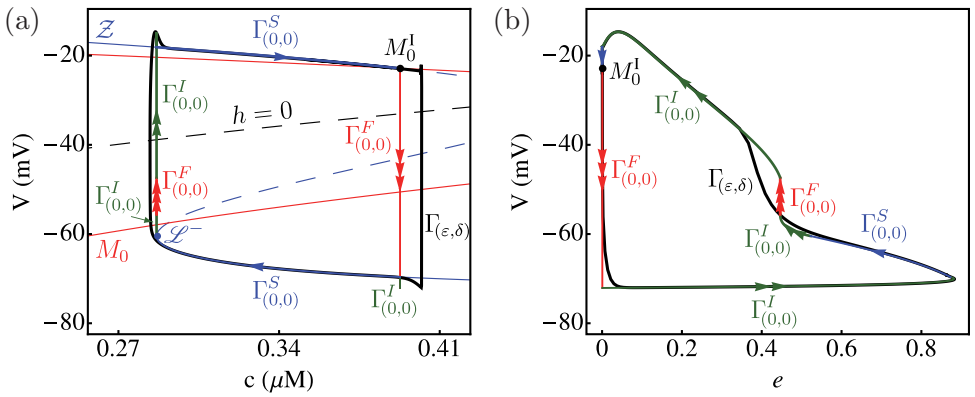

Figure 10. *Singular orbit construction for a dynamic MMO with $g_K = 3$ nS, $g_{BK} = 0.4$ nS, and $g_A = 8$ nS (cf. Figures 5 and 6, panels* (c) *and* (d)*). A solution $\Gamma_{(\varepsilon,\delta)}$ (black) of (2.2) for $C_m = 0.2$ pF and $f_c = 0.001$ is shown along with the singularities $\mathcal{Z}$ and M_0 of (6.2). There are three FSN* I *points (only one of which is labeled M_0^I). The singular MMO is a concatenation of seven distinct orbit segments.*

in this region. The third singularity in our attractor is the FSN I point M_0^{I}, which is new and specific to 3-timescale problems. The small oscillations of the fully perturbed MMO occur in a neighborhood of this FSN I point. Naively, we would expect the oscillation mechanism to be related to folded singularities. This is only partly true. We defer detailed discussion of how the FSN I point M_0^{I} unfolds to section 7.

As is clear from Figure 10, the limiting subsystems are an excellent approximation of the fully perturbed problem. Away from the singularities $\mathscr{L}^-$, L, and M_0^{I}, the full system trajectory $\Gamma_{(\varepsilon,\delta)}$ is $\mathcal{O}(\varepsilon)$ close to $\Gamma^F_{(0,0)} \cup \Gamma^I_{(0,0)}$. As in section 6.2, the perturbative effects of ε and δ are nonuniform and δ has very weak influence on the shape of trajectories around the fast-intermediate timescale transition. Similarly, $\Gamma_{(\varepsilon,\delta)}$ is $\mathcal{O}(\delta)$ close to $\Gamma^I_{(0,0)} \cup \Gamma^S_{(0,0)}$ and ε has virtually no effect on the shape of orbits around the intermediate-slow timescale transition. The singular dynamic MMO attractor is a hysteresis cycle that alternates between stable branches of $\mathcal{Z}$ (and S). The benefit of the 3-timescale splitting is that we have access to additional information about the shape of the trajectory that we did not have in the 2-timescale splittings. On the other hand, the 3-timescale decomposition retains the degeneracies of the 1-fast/3-slow and 3-fast/1-slow methodologies, making the singular orbit construction more difficult.

6.4. Calcium-conducting bursts. The geometric configuration of $\mathcal{Z}$ is an important factor in determining the type of MMO attractor. As we saw in section 5.3, parameter variations alter the structure of $\mathcal{Z}$ and when bistability of $\mathcal{Z}$ no longer holds, the MMO attractor changes dramatically. To reiterate the main points of section 5.3, there was a torus of stable singular MMOs between the fold point $\mathscr{L}^-$ and the Hopf point $\mathcal{Z}^H$. The unique attractor was situated somewhere between these two points. The method of averaging was identified as the appropriate analytic tool to locate the MMO attractor.

These properties persist in the double limit $(\varepsilon, \delta) \to (0, 0)$ with the Hopf bifurcation $\mathcal{Z}^H$ replaced by the FSN I point M_0^{I} (Figure 11). The net effect of the averaging process is to remove the slowest variable so that the remaining (V, n, e) subsystem is a classic 2-

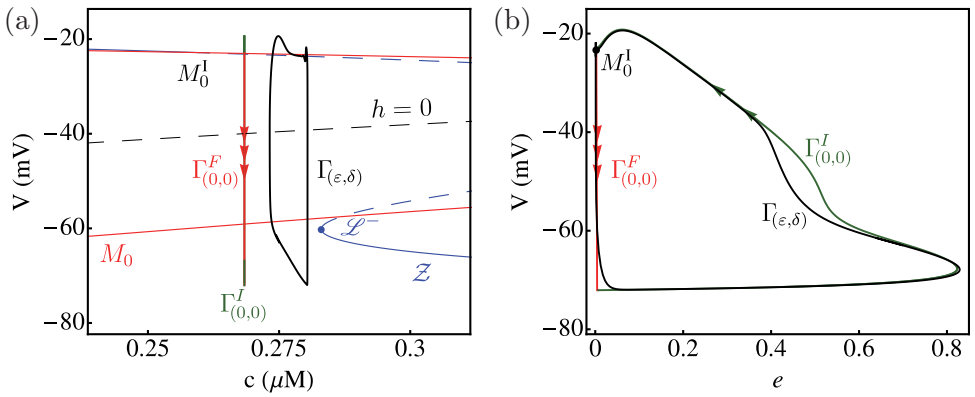

Figure 11. *Singular orbit construction via averaging for a calcium-conducting MMO. The parameters are* $g_K = 5$ nS, $g_{BK} = 0.4$ nS, *and* $g_A = 8$ nS *(cf. Figures* 5(e)–(f) *and* 8(b)–(c)*) with* $C_m = 0.2$ pF *and* $f_c = 0.001$ *for the full system trajectory. The oscillation region is bordered by the fold point* $\mathscr{L}^-$ *and the FSN* I *point* M_0^I.

timescale problem. We immediately inherit the results established in [60, 61], which we briefly summarize here. The singular orbit $\Gamma^F_{(0,0)} \cup \Gamma^I_{(0,0)}$ is an alternation between intermediate and fast orbit segments that jump at a folded node. The singular orbit satisfies the criteria for a canard-induced MMO: the presence of a folded node and a global reinjection mechanism that resets the system dynamics after passage through the canard point [9].

The appearance of the small amplitude oscillations in the calcium-conducting MMOs can then be explained by examining the geometry of the (V, n, e) subsystem away from the singular limit $\varepsilon = 0$. The normally hyperbolic regions of S perturb to invariant slow manifolds $S^a_{(\varepsilon,0)}, S^r_{(\varepsilon,0)}$, which are $\mathcal{O}(\varepsilon)$ close to their singular limit counterparts. Extension of the invariant slow manifolds by the flow of (2.2) with $\delta = 0$ into the vicinity of the folded node results in a local twisting of the attracting and repelling sheets [49, 62]. These rotations occur in an $\mathcal{O}(\varepsilon^{1/2})$ neighborhood of the folded node with maximum amplitude of size $\mathcal{O}(\varepsilon^{1/2})$. We illustrate this in Figure 12 by showing how the attracting and repelling manifolds S^a and S^r unfold for nonzero ε. The numerical method used to compute the attracting and repelling slow manifolds involves reformulating (2.2) with $\delta = 0$ as a boundary value problem and using homotopic continuation to generate a family of solutions that form a mesh of the surface. We refer the reader to [11, 12, 13] for details of the method with examples and to the AUTO demo files [16], which provide sample codes.

Remark 6.4. In comparing Figures 11(a) and 8(b), it is clear that the averaged singular MMO undergoes a leftward shift as $\varepsilon \to 0$. This can be explained using canard theory. Note in (5.7) that the averaging takes the ε dependence into consideration. As a result, the averaged orbit computed in section 5.3 fully accounts for the slow passage effects induced by the canard dynamics in the active phase. As $\varepsilon \to 0$, however, the small oscillations near the folded node disappear (recall the $\mathcal{O}(\varepsilon^{1/2})$ dependence) and the time spent in the active phase is underestimated. Consequently, as $\varepsilon \to 0$, the silent phase has a greater contribution than the active phase to the averaged orbit and the singular MMO shifts to lower c values.

The rotational properties of the slow manifolds are closely related to the existence of canards in (2.2) with $\delta = 0$. Canards are trajectories that cross from $S^a_{(\varepsilon,0)}$ to $S^r_{(\varepsilon,0)}$ and

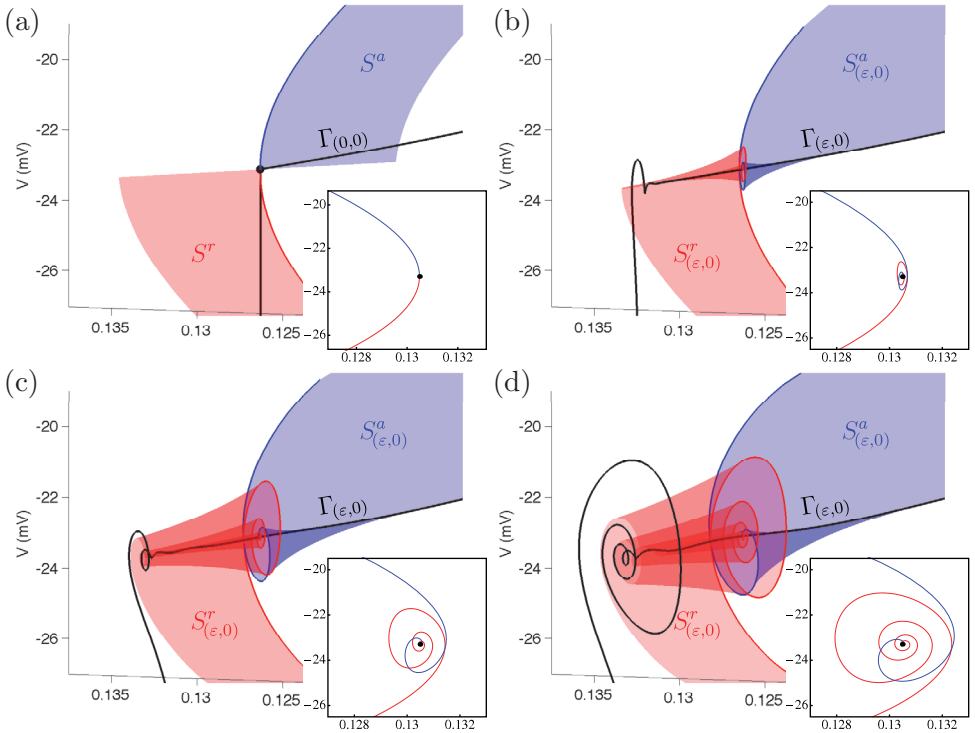

Figure 12. *Unfolding of the slow attracting (blue) and repelling (red) manifolds for fixed $c = \overline{c}$, calculated up to a section passing through the folded node. The insets show the intersection of the manifolds with a hyperplane through the folded node. The maximal canards correspond to the intersections of the attracting and repelling surfaces. Parameter values are as in Figure 11 with* (a) $C_m = 0$ pF, (b) $C_m = 0.1$ pF, (c) $C_m = 0.5$ pF, *and* (d) $C_m = 1$ pF.

remain $\mathcal{O}(\varepsilon)$ close to $S^r_{(\varepsilon,0)}$ for $\mathcal{O}(1)$ times on the intermediate timescale. Maximal canards are transverse intersections of the slow attracting and repelling manifolds extended beyond the fold surface L. Two particularly important canard solutions are the *strong canard*, γ_0, and the *weak canard*, γ_w, which correspond to the strong and weak eigendirections of the folded node. The strong canard is easily identified as the first (or outermost) intersection of the slow manifolds and marks the onset of oscillatory behavior. Trajectories on either side of γ_0 either simply jump off the repelling manifold or undergo small oscillations before jumping off $S^r_{(\varepsilon,0)}$. The weak canard is the last (or innermost) intersection of the slow manifolds and is the axis of rotation for both the canards and the invariant manifolds [62, 11, 13]. Furthermore, the canards shape the phase space in the sense that a trajectory lying between the nth and $n+1$st maximal canards makes n small oscillations before it is repelled.

Recall from section 5.3 that the transient evolution to the calcium-conducting MMO attractor exhibited a wide variety of bursts. The 3-timescale decomposition gives us access to canard theory, allowing for a complete explanation of the transient behavior. For the parameter set in Figure 11, we find that the eigenvalue ratio of the folded node of the attractor is $\mu \approx 0.041$ and $s_{\max} = 12$. At the FSN I point M_0^{I}, the eigenvalue ratio μ is zero. As c increases, μ increases until it eventually reaches $\mu = 1$ (beyond the fold point $\mathscr{L}^-$), where the

folded nodes of M_0 become folded foci. Transients of (2.2) that pass through a neighborhood of M_0^{I} undergo a large number of small oscillations. As the trajectory slowly drifts towards the attractor, it encounters a different folded node (with larger μ) every time it returns to M_0. Thus, the maximal number of small oscillations gradually decreases until the attractor is reached (see Figure 7(a)). A similar argument shows that there is a monotonic increase (until the attractor is reached) in the number of subthreshold oscillations for those transients of (2.2) that approach the attractor via the fold point $\mathscr{L}^-$.

Remark 6.5. An understanding of the transient evolution allows us to predict how our model system responds to external stimuli such as a calcium pulse. We contend that this can be experimentally significant since the transient evolution can distinguish between the two MMO types. Transients featuring pseudo-plateau bursts with a wide variety of small oscillations are associated with calcium-conducting MMOs. Meanwhile, transients that simply decay to a slow flow along $\mathcal{Z}$ are characteristic features of dynamic MMOs.

Thus, the 3-timescale decomposition provides the geometric information necessary to identify calcium-conducting MMOs and the theoretical framework (canard theory) to explain their oscillatory behavior. We observe that when there is no bistability, the singular MMO construction consists only of intermediate and fast orbit segments. In other words, since we can average out the c-dynamics, we are effectively down to a 2-timescale problem.

6.5. Spiking orbits. Spiking behavior always falls (for sufficiently small ε) into parameter regimes where there is no bistability of $\mathcal{Z}$ and we are able to discard a slow direction (via averaging). Consequently, we again deal with a family of 2-timescale problems with parameter c. To determine the difference between spiking and bursting, we first note that the curve of folded singularities M_0 possesses degenerate folded nodes (DFNs), where folded nodes turn into folded foci. Obviously, if the averaged singular attractor is fixed at a c value such that M_0 has a folded focus, then the corresponding full system trajectory will be a spiking pattern. If the averaged singular attractor has a c value such that M_0 has a folded node, there is no guarantee that the singular orbit will converge to that folded node. Recall that associated with each folded node is a trapping region called the funnel, delimited by the strong canard and by the fold surface L. Trajectories that land inside the funnel inevitably pass through the folded node. Trajectories that land outside the funnel encounter the fold surface L at a jump point instead. The beauty of the double limit $(\varepsilon, \delta) \to (0, 0)$ is that the funnel region (and the spiking/bursting criterion) can be visualized (Figure 13).

In Figure 13(a), the averaged singular orbit has $\overline{c} \approx 0.2245$ μM and the associated folded singularity has complex eigenvalues. The corresponding singular attractor $\Gamma^F_{(0,0)} \cup \Gamma^I_{(0,0)}$ with $c = \overline{c}$ is a typical relaxation oscillator. For the example in Figure 13(a), the singular orbit does not actually hit the upper fold at the folded focus but at a regular jump point. The associated time trace of (2.2) shown in Figure 13(c) is a spiking pattern, as expected. In Figure 13(b), the singular attractor has $\overline{c} \approx 0.2467$ μM and M_0 possesses a folded node with eigenvalue ratio $\mu \approx 0.555$ (and $s_{\max} = 1$). In this case, the fast up-jump projects the singular orbit into the funnel region of the folded node. That is, we have a folded node and a global reinjection mechanism (fast depolarization) that returns trajectories to the funnel region. The associated full system trajectory is an MMO with 1 small oscillation (Figure 13(d)) in accordance with the theoretical prediction.

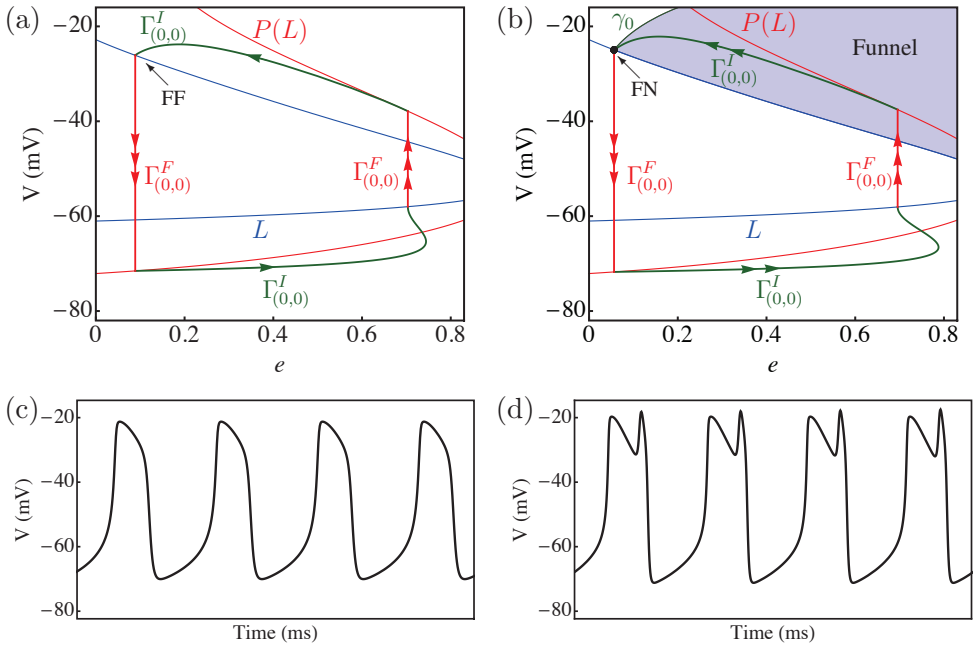

Figure 13. *The difference between spiking and bursting for* $g_{BK} = 0.4$ nS, $g_A = 4$ nS, *and* (a) $g_K = 9$ nS *and* (b) $g_K = 7$ nS. *Panels* (a) *and* (b) *are projections into the* (V, e) *plane. For fixed* c, *the fold surface* L *is a curve (blue). Its projection* $P(L)$ *(red) onto different branches of* S *is shown to indicate where fast orbit segments land. In* (a), *the singular attractor hits the folds at regular jump points and the full system orbit (for* $C_m = 2$ pF *and* $f_c = 0.001$*) is a relaxation oscillation (panel* (c)*). In* (b), *the singular attractor is inside the funnel of the folded node and the full system trajectory is a* 1^1 *MMO (panel* (d)*).*

6.6. Bifurcation diagrams. We have shown that the 3-timescale splitting can be used as an effective predictor to explain both the transient dynamics and attractors of (2.2). Our central concern is in identifying the various mechanisms that cause the observed dynamical behaviors (particularly the bursting). We do this by constructing singular two-parameter diagrams (shown in Figures 4(a), (c), and (e)). The singular two-parameter diagrams are divided into three regions, reflecting the different attractors. The sector marked "Dep" represents the subset of parameter space where the depolarized steady state is the attractor. The "Delayed Hopf"' region corresponds to the dynamic MMOs. The "Calcium-conducting" region corresponds to the MMOs where averaging can be used to fix the calcium. The singular spiking orbits lie in the spiking region.

The boundary between the equilibrium state and the singular MMO state is the set of FSN II points E_{SHB}, where the equilibrium crosses from an attracting manifold S^a (and $\mathcal{Z}^a$) to a repelling manifold S^r (and $\mathcal{Z}^r$). The subdivision between dynamic and calcium-conducting MMOs within the MMO regime is related to the geometric structure of the critical manifold $\mathcal{Z}$. When the stable branches of $\mathcal{Z}$ overlap (denoted "Delayed Hopf" in Figure 4), the singular MMO attractor is a hysteresis cycle. The small oscillations occur in a neighborhood of M_0^{I}, but the precise oscillation mechanism is still unknown. When the stable branches of $\mathcal{Z}$ are separated (labeled "Calcium-conducting"), the calcium variable can be fixed and the small amplitude oscillations are associated with a folded node singularity. The degeneracy where

the c-coordinate of $\mathscr{L}^-$ and M_0^{I} coincide (labeled "Bistability") approximates the boundary between dynamic and calcium-conducting MMOs.

To complete our singular two-parameter diagrams, we must locate the border between the calcium-conducting MMOs and spiking orbits. The singular spiking attractor can be associated with either a folded focus or a folded node. In the case of a folded node, the singular orbit lands outside the funnel of the folded node. Thus, there are two parts to the border between the singular spiking and MMO orbits. One part of the spiking/MMO boundary consists of the set of singular orbits that jump at a DFN. The other segment of the spiking/MMO boundary is the set of singular orbits associated with folded nodes that land neither inside nor outside the funnel; i.e., they land on the strong canard itself. Figure 4 clearly demonstrates that our singular subsystems provide a good first approximation to the dynamics of the fully perturbed problem for sufficiently small (ε, δ).

By using the multiple timescale structure of (2.2) to our advantage, we can explain the dynamics of (2.2). Canard theory in the 1-fast/3-slow approach provides the theoretical basis for the oscillation mechanism. Geometric considerations in the 3-fast/1-slow approach generate a criterion to identify the MMO type. The 3-timescale splitting then gives the best of both worlds and allows the construction of diagrams such as Figure 4, which elucidate the cause of the observed attractors of (2.2). However, there are setbacks to the 3-timescale approach. The most obvious is that the dynamic MMOs jump at the FSN I point M_0^{I}, which is a doubly degenerate point where M_δ^{II} and $\mathcal{Z}^H$ merge. The rest of the paper is concerned with unravelling the oscillation mechanism of dynamic MMOs.

7. The oscillation mechanism.

We have seen that the complex oscillatory waveforms in (2.2) can manifest as MMOs of either dynamic or calcium-conducting type. In the calcium-conducting case, the small oscillations in the bursts were unequivocally identified as canards. In the dynamic MMO case, the precise oscillation mechanism depends on the chosen geometric viewpoint. The 1-fast/3-slow formulation suggests that the subthreshold oscillations are due to canards, while the 3-fast/1-slow viewpoint insists that the oscillations are due to a slow passage through a dynamic Hopf bifurcation. In this section we examine the oscillation mechanism for dynamic MMOs more carefully and reconcile the seeming discrepancy.

7.1. Perturbations of the FSN I point M_0^{I}.

In section 6 we showed that when bistability of the critical manifold $\mathcal{Z}$ holds, the resulting oscillatory behavior of (2.2) can be attributed to the degenerate FSN I point M_0^{I}. In section 4 we found that the oscillations were associated with folded node singularities with $\mu \approx 0$. More specifically, there was always an FSN I M_δ^{I} that was $\mathcal{O}(\delta)$ close. In section 5, the oscillatory behavior emerged from neighborhoods of a Hopf bifurcation $\mathcal{Z}^H$ that was $\mathcal{O}(\varepsilon)$ close to the fold surface L. In Appendix B, we show that M_δ^{I} and $\mathcal{Z}^H$ are different unfoldings of the FSN I point M_0^{I}. However, it is beyond our scope to analyze how trajectories perturb in both ε and δ. We conjecture that if δ is sufficiently small, then the small oscillations of the fully perturbed problem inherit their rotational properties from the dynamic Hopf bifurcation. Alternatively, if δ is sufficiently large, the rotational properties of trajectories are manifestations of the properties of the canards.

Figure 14 shows the effect of "small" and "large" δ on trajectories of the fully perturbed problem (2.2). In panel (a), δ is small enough that the 3-fast/1-slow splitting is valid. The slow drift in the calcium variations moves the trajectory through the Hopf bifurcation. As a

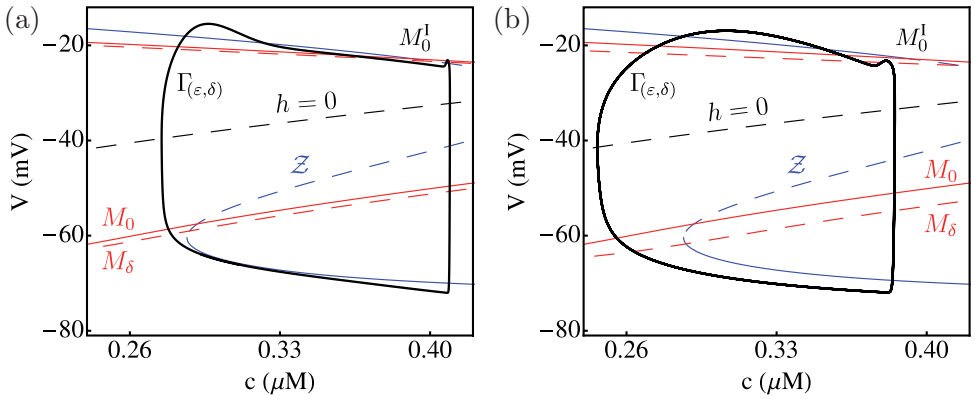

Figure 14. *Oscillatory behavior associated with the FSN* I *point* M_0^I *for various* δ. *The parameters are* $g_K = 3$ nS, $g_{BK} = 0.4$ nS, $g_A = 8$ nS, $C_m = 0.2$ pF, *and* (a) $f_c = 0.01$ *or* (b) $f_c = 0.03$. *The singularities* $\mathcal{Z}$ *and* M_0 *(red, solid) of* (6.2) *are shown along with the folded singularities* M_δ *(red, dashed) of* (4.6). (a) *When* δ *is small, the trajectories exhibit properties of the Hopf.* (b) *When* δ *is large, the trajectories no longer stick to* $\mathcal{Z}$ *and the small oscillations arise from canards.*

result, we see trajectories typical of a delayed Hopf. By increasing the perturbation parameter δ, we eventually cross a secondary bifurcation and the nature of the orbit changes. Panel (b) shows the trajectory after the secondary bifurcation has been crossed. The trajectory no longer closely follows the manifold $\mathcal{Z}$. Clearly, $\Gamma_{(\varepsilon,\delta)}$ undergoes its small oscillations in a neighborhood of M_δ (about a folded node). Thus, by increasing δ, we have moved from a parameter regime where the 3-fast/1-slow splitting is favored to a regime where the 1-fast/3-slow splitting is appropriate.

7.2. Delayed Hopf bifurcation and tourbillon. There exists a subset of parameter space such that the dynamic MMOs exhibit oscillations above an observable threshold. Such dynamic MMOs are called a *tourbillon* [14]. The burst patterns associated with a tourbillon are qualitatively different from those arising from delayed Hopf or folded node mechanisms (see Figure 15). Despite this, a tourbillon is actually just a different manifestation of a dynamic Hopf bifurcation. Recall that MMOs approaching the Hopf $\mathcal{Z}^H$ from an $\mathcal{O}(1)$ distance become exponentially close to $\mathcal{Z}_{(\varepsilon,0)}$ and so display virtually no small oscillations. In the case of a tourbillon, the trajectory approaches the dynamic Hopf bifurcation from a much closer distance. In that case, the real part of the eigenvalues is small and the attraction to $\mathcal{Z}_{(\varepsilon,0)}$ is weak. As a result, the trajectory does not have sufficient time to be exponentially attracted and the oscillations are visible throughout. The speed at which the trajectory traverses the dynamic Hopf region is governed by the slowest timescale. As δ increases, the time spent near the Hopf decreases, and hence the number of observed oscillations decreases.

Figure 15 illustrates the difference between the two types of trajectories that pass by a dynamic Hopf bifurcation. Panel (a) depicts a geometric configuration in which the lower fold point $\mathscr{L}^-$ and the FSN I point M_0^{I} are well separated. This means that the full system bursting attractor shows virtually none of its subthreshold oscillations. The only observable small oscillation is at the end of the oscillatory regime when the trajectory jumps off the slow manifold. Figure 15(b) shows that when $\mathscr{L}^-$ and M_0^{I} are not well separated, the hys-

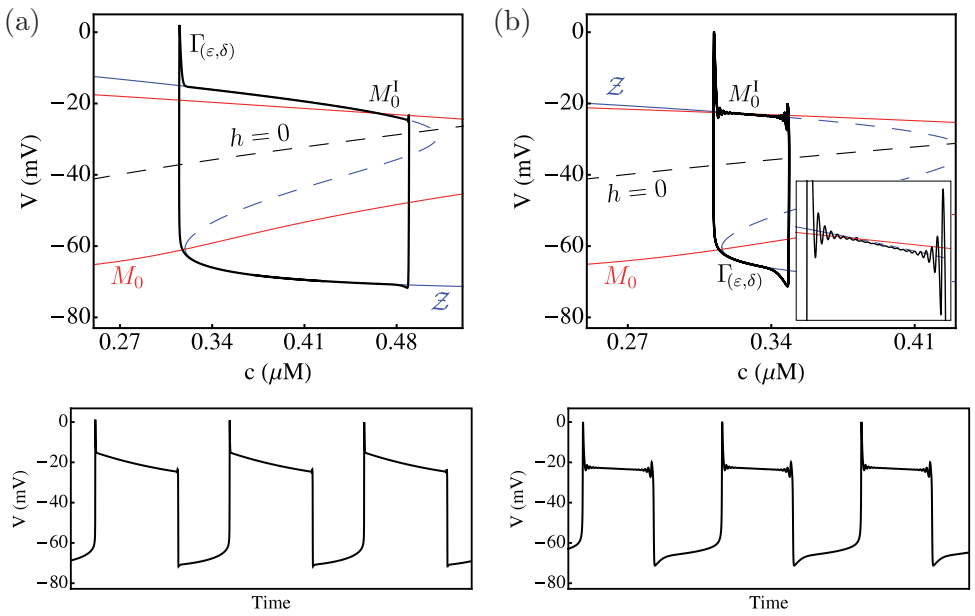

Figure 15. *The two types of dynamic Hopf bifurcation for* $g_{BK} = 0.4$ nS, $g_A = 4$ nS*:* (a) *delayed Hopf bifurcation* ($g_K = 2$ nS) *and* (b) *tourbillon* ($g_K = 4$ nS). *Full system trajectories (black) have* $C_m = 2$ pF *and* $f_c = 0.001$.

teresis loop narrows in width when viewed in the (V, c) projection. This means trajectories return sufficiently close to the Hopf that the rotations occur before the the trajectory can be exponentially attracted to the slow manifold. The amplitude of the small oscillations in a tourbillon initially decreases and eventually increases before the trajectory jumps away. This is because the real part of the eigenvalues is initially negative and increases through zero to positive values where the manifold becomes repelling.

It becomes clear that when the parameters are chosen such that bistability holds and the fold point $\mathscr{L}^-$ and the FSN I point M_0^{I} are weakly separated, the resulting full system trajectory will (in principle) be a tourbillon. However, for fixed ε, the difference between a tourbillon and a delayed Hopf MMO is not always clear. There is no predefined distance that can be used to differentiate between the two types of dynamic Hopf phenomena.

8. Discussion. MMOs are complex oscillatory waveforms characterized by an alternation between large and small amplitude oscillatory motion. Often appearing in the time course evolution of neural bursting models, MMOs have become a new metric in neuroscience [18]. As a result, a thorough understanding of the structure of MMOs and their mechanisms has become a significant interdisciplinary endeavor. An important aspect of MMOs is the multiscale structure of their governing equations, making them amenable to singular perturbation methods. One particular singular perturbation technique that has been used with great success is geometric singular perturbation theory. Using this geometric approach, we have examined the transient and long-term dynamics of a 3-timescale neuroendocrine cell model (2.2). Our results show that the early investigations of (2.2) produced limited, nonoverlapping views of the mixed mode dynamics in the pituitary cell model.

The dynamics of pseudo-plateau bursting have been of interest to both the cell modeling community and to those interested in MMOs in multiscale systems. Historically, the analysis of bursting in slow/fast systems was pioneered by [40], and several treatments of pseudo-plateau bursting followed suit [38, 39, 47, 56]. In this traditional 3-fast/1-slow approach, the small oscillations are born from a slow passage through a dynamic Hopf bifurcation [36, 37, 3] and the MMOs are hysteresis loops that alternately jump at a fold and a subcritical Hopf (fold/sub-Hopf bursts) [41, 24]. We extended the standard slow/fast analysis and computed the additional MMO families that bifurcate from the unstable spiking branch (Figure 8). This classic slow/fast analysis is particularly effective for dynamic MMOs and for detecting the switch from dynamic to calcium-conducting MMOs. Away from singularities of the slow and "fast" subsystems, Fenichel theory guarantees that the singular and nonsingular orbits are $\mathcal{O}(\delta)$ close to each other.

An alternative and more recent take on pseudo-plateau bursting complements the classic approach. In the 1-fast/3-slow analysis, a folded critical manifold and canard orbits shape the dynamics. This novel slow/fast analysis is particularly effective in explaining the oscillatory behavior of calcium-conducting MMOs. We showed that other geometric features, such as a curve of cusp bifurcations, could influence the resetting behavior of MMOs via fast depolarization at a fold or via circumnavigation of the cusps. The full system trajectories were $\mathcal{O}(\varepsilon)$ perturbations of the singular limit predictions in regions of normal hyperbolicity [19, 26]. In a neighborhood of the fold surface L or a folded node, the asymptotic error estimates were $\mathcal{O}(\varepsilon^{2/3})$ [30, 50] and $\mathcal{O}(\varepsilon^{1/2})$ [9, 62], respectively. Our work also adds to the currently scarce supply of examples of canard-induced MMOs in systems with more than two slow variables [22, 23]. In both the 3-fast/1-slow and 1-fast/3-slow analyses, the underlying geometry influences the bursting through a combination of local and global mechanisms. These two slow/fast analyses of (2.2) stem from the inherent 3-timescale structure.

The core focus of our work has been the comparison of the relative strengths and weaknesses of these two complementary geometric methods in the context of the 3-timescale singular perturbation problem (2.2). When dealing with such problems, there are always questions of which analysis is appropriate and how the different methods are related [52]. In this work, we have directly addressed how the classic and novel 2-timescale methods are related in the context of system (2.2). To be precise, they are different unfoldings of the more degenerate 3-timescale decomposition. As to the question of which method is most appropriate, we assert that the 3-timescale decomposition provides the best results asymptotically, independent of the model, as it inherits all of the geometric information contained in the different 2-timescale analyses. As a result, the 3-timescale decomposition provides us with a remarkable degree of control and predictive power.

To the authors' knowledge, there has been little work done on 3-timescale problems [25, 28, 29]. In this article, we have concentrated on 3-timescale problems of the form (1.1), in which there is an obvious ordering of the timescales, i.e.,

$$\delta \ll 1 \ll \frac{1}{\varepsilon}.$$

In particular, we analyzed a 3-timescale pituitary lactotroph model using geometric singular perturbation analysis techniques. We have demonstrated the potency of such an approach

and formulated our analysis in a general way that easily carries over to other 3-timescale problems. Our analysis showed that, for the most part, each transition of a trajectory could be explained locally by the interaction of 2-timescales only. However, we have also shown that there is a need for the development of a comprehensive theoretical framework for 3-timescale systems. In the 3-timescale formulation, we encountered degeneracies not yet seen before in the form of the FSN I points M_0^{I}, which represent the interaction of objects from the 3-fast/1-slow theory (the critical manifold $\mathcal{Z}$) with objects from the 1-fast/3-slow theory (the folded singularities M_0). The unfolding of M_0^{I} is particularly important because it is new and it marks regions in phase space where all three timescales interact. Moreover, there are elements of the 2-timescale theory that require deeper analysis. For instance, the unfolding of FSN type I singularities via blow-up and complex time path analysis has yet to be done [31], and our work demonstrates that it is becoming a priority. In any case, we have shown that there is great benefit in combining geometric singular perturbation theory with bifurcation analysis. The moral of the story, then, is that it never hurts to look at a problem from multiple points of view.

Appendix A. The pituitary lactotroph model. The mathematical model we study is a 4D dynamical system describing the electrical activity and calcium signaling in a pituitary lactotroph cell [51]. The model equations are provided in (2.1). The ionic currents are as given in section 2, and the steady state functions are given by

$$
\begin{aligned}
x_\infty(V) &= \left[1+\exp\left(\frac{V_x - V}{s_x}\right)\right]^{-1},\\
e_\infty(V) &= \left[1+\exp\left(\frac{V - V_e}{s_x}\right)\right]^{-1},\\
s_\infty(c) &= \frac{c^2}{c^2+k_s^2},
\end{aligned}
$$

where $x \in \{m, n, f, a\}$. Standard parameter values are provided in Table 1.

Appendix B. The FSN I point M_0^{I}. In [63], the canard theory of singularly perturbed problems is extended to the general case of k slow and m fast variables, with $k \geq 2$ and $m \geq 1$. We restate Theorem 3.1 of [63], as it applies to our problem. Suppose we have a standard 2-timescale singularly perturbed problem with a locally folded m-dimensional critical manifold S with an $(m-1)$-dimensional manifold of fold points. Suppose further that S possesses an $(m-2)$-dimensional set of generic folded singularities and that the $(m-1)$ nonzero eigenvalues of S along the fold have negative real part. Then there exists (after center manifold reduction) a smooth change of coordinates that transforms the standard slow/fast system to

$$
\begin{aligned}
\varepsilon\,\dot{x} &= y_1(1+x\mathcal{O}(y_2,z)) + x^2(1+\mathcal{O}(x,y_1)) + \varepsilon\,\mathcal{O}(x,y_1,y_2,\varepsilon),\\
\dot{y}_1 &= B_2(z)y_2 + C(z)x + \mathcal{O}(y_1,x^2,y_2^2,xy_2) + \varepsilon\,\mathcal{O}(x,y_1,y_2,z),\\
\dot{y}_2 &= A_2(z) + \beta_2 y_2 + \mathcal{O}(x,y_1,\varepsilon),\\
\dot{z} &= A_3(z) + \mathcal{O}(x,y_1,y_2,\varepsilon),
\end{aligned}
\tag{B.1}
$$

Table 1

System parameters for the pituitary lactotroph model (2.1).

Parameter	Value	Definition
C_m	$0-10$ pF	Membrane capacitance
g_{Ca}	2 nS	Maximal conductance of Ca^{2+} channels
V_{Ca}	50 mV	Reversal potential for Ca^{2+}
V_m	-20 mV	Voltage value at midpoint of m_∞
s_m	12 mV	Slope parameter of m_∞
g_K	$0-10$ nS	Maximal conductance of delayed rectifier K^+ channels
V_K	-75 mV	Reversal potential for K^+
V_n	-5 mV	Voltage value at midpoint of n_∞
s_n	10 mV	Slope parameter of n_∞
τ_n	30 ms	Time constant for n
λ	0.7	Parameter used to control spiking pattern
g_{BK}	$0-0.7$ nS	Maximum conductance of BK-type K^+ channels
V_f	-20 mV	Voltage value at midpoint of f_∞
s_f	5.6 mV	Slope parameter of f_∞
g_{SK}	1.7 nS	Maximum conductance of SK channels
k_s	0.5 μM	c at midpoint of s_∞
g_A	$0-25$ nS	Maximal conductance of A-type K^+ channels
V_a	-20 mV	Voltage value at midpoint of a_∞
s_a	10 mV	Slope parameter of a_∞
V_e	-60 mV	Voltage value at midpoint of e_∞
s_e	10 mV	Slope parameter of e_∞
τ_e	20 ms	Time constant of e
f_c	0.01	Fraction of free Ca^{2+} ions in cytoplasm
α	0.0015 μMfC^{-1}	Conversion from charge to concentration
k_c	0.16 ms^{-1}	Rate of Ca^{2+} extrusion

where

$$A_j(z) = a_j + g_{j,1}(z),$$
$$B_2(z) = b_2 + g_{1,1}(z),$$
$$C(z) = c + g_{1,2}(z),$$

with $g_{i,j}(0) = 0$ and computable constants $a_2, a_3, b_2, c, \beta_2$, which are generically nonzero.

Using (B.1) as our starting point, we wish to compute a canonical form for an FSN I point M_0^{I}. Without loss of generality, we assume the curves $\mathcal{Z}$ and M_0 cross at the origin (i.e., M_0^{I} is at the origin). This requires $a_2 = 0$ and $a_3 = 0$. We also assume that the folded singularities change from folded nodes (with two negative real eigenvalues) to folded saddles at the FSN I point. A sufficient condition for this is $C(z) < 0$ in a neighborhood of the origin.

The critical manifold $\mathcal{Z}$ is given parametrically by

$$\mathcal{Z} = \left\{ x = \frac{A_2(z)B_2(z)}{\beta_2 C(z)},\ y_1 = -\frac{A_2^2(z)B_2^2(z)}{\beta_2^2 C^2(z)},\ y_2 = -\frac{A_2(z)}{\beta_2} \right\},$$

and the curve of folded singularities is defined by

$$M = \{x = 0, y_1 = 0, y_2 = 0\}.$$

A Hopf bifurcation of the (x, y_1, y_2) subsystem is given by the condition

$$A_2(z)B_2(z)\left(2A_2(z)B_2(z) - C^2(z) + \varepsilon\,\beta_2^2 C(z)\right) = 0,$$

together with

$$C(z)\left(2A_2(z)B_2(z) - C^2(z)\right) > 0.$$

The nonzero eigenvalues of the desingularized system of (B.1) with $a_2 = 0$, $a_3 = 0$ are given by

$$2\lambda = C(z) \pm \sqrt{C^2(z) - 8A_2(z)B_2(z)}.$$

We thus have both a Hopf bifurcation of the (x, y_1, y_2) subsystem and an FSN of the desingularized system as we pass through M_0^{I} (i.e., as $A_2(z) \to 0$).

Acknowledgments. TV thanks RB and Florida State University for their hospitality, where part of this work was completed. The authors also thank the anonymous referees, whose comments and ideas helped clarify the text.

REFERENCES

[1] S. M. Baer and T. Erneux, *Singular Hopf bifurcation to relaxation oscillations*, SIAM J. Appl. Math., 46 (1986), pp. 721–739.

[2] S. M. Baer and T. Erneux, *Singular Hopf bifurcation to relaxation oscillations* II, SIAM J. Appl. Math., 52 (1992), pp. 1651–1664.

[3] S. M. Baer, T. Erneux, and J. Rinzel, *The slow passage through a Hopf bifurcation: Delay, memory effects, and resonance*, SIAM J. Appl. Math., 49 (1989), pp. 55–71.

[4] R. Bertram, M. J. Butte, T. Kiemel, and A. Sherman, *Topological and phenomenological classification of bursting oscillations*, Bull. Math. Biol., 57 (1995), pp. 413–439.

[5] R. Bertram and A. Sherman, *Negative calcium feedback: The road from Chay-Keizer*, in The Genesis of Rhythm in the Nervous System, S. Coombes and P. Bressloff, eds., World Scientific, Hackensack, NJ, 2005, pp. 19–48.

[6] J. Best, A. Borisyuk, J. Rubin, D. Terman, and M. Wechselberger, *The dynamic range of bursting in a model respiratory pacemaker network*, SIAM J. Appl. Dyn. Syst., 4 (2005), pp. 1107–1139.

[7] H. W. Broer, T. J. Kaper, and M. Krupa, *Geometric Desingularization of a Cusp Singularity in Slow-Fast Systems with Applications to Zeeman's Examples*, preprint.

[8] M. Brøns, T. J. Kaper, and H. G. Rotstein, *Introduction to focus issue: Mixed mode oscillations: Experiment, computation, and analysis*, Chaos, 18 (2008), 015101.

[9] M. Brøns, M. Krupa, and M. Wechselberger, *Mixed mode oscillations due to the generalized canard phenomenon*, in Bifurcation Theory and Spatio-temporal Pattern Formation, Fields Inst. Commun. 49, AMS, Providence, RI, 2006, pp. 39–63.

[10] C. A. Del Negro, C. F. Hsiao, and S. H. Chandler, *Outward currents influencing bursting dynamics in guinea pig trigeminal motoneurons*, J. Neurophysiol., 81 (1999), pp. 1478–1485.

[11] M. Desroches, B. Krauskopf, and H. M. Osinga, *The geometry of slow manifolds near a folded node*, SIAM J. Appl. Dyn. Syst., 7 (2008), pp. 1131–1162.

[12] M. Desroches, B. Krauskopf, and H. M. Osinga, *Mixed-mode oscillations and slow manifolds in the self-coupled FitzHugh-Nagumo system*, Chaos, 18 (2008), 015107.

[13] M. Desroches, B. Krauskopf, and H. M. Osinga, *Numerical continuation of canard orbits in slow-fast dynamical systems*, Nonlinearity, 23 (2010), pp. 739–765.

[14] M. Desroches, J. Guckenheimer, B. Krauskopf, C. Kuehn, H. M. Osinga, and M. Wechselberger, *Mixed-mode oscillations with multiple time scales*, SIAM Rev., 54 (2012), pp. 211–288.

[15] E. J. Doedel, *AUTO: A program for the automatic bifurcation analysis of autonomous systems*, Congr. Numer., 30 (1981), pp. 265–284.

[16] E. J. Doedel, A. R. Champneys, T. F. Fairgrieve, Y. A. Kuznetsov, K. E. Oldeman, R. C. Paffenroth, B. Sanstede, X. J. Wang, and C. Zhang, *AUTO-07P: Continuation and Bifurcation Software for Ordinary Differential Equations*, http://cmvl.cs.concordia.ca/(2007).

[17] J. Drover, J. Rubin, J. Su, and B. Ermentrout, *Analysis of a canard mechanism by which excitatory synaptic coupling can synchronize neurons at low firing frequencies*, SIAM J. Appl. Math., 65 (2004), pp. 69–92.
[18] I. Erchova and D. J. McGonigle, *Rhythms of the brain: An examination of mixed mode oscillation approaches to the analysis of neurophysiological data*, Chaos, 18 (2008), 015115.
[19] N. Fenichel, *Geometric singular perturbation theory for ordinary differential equations*, J. Differential Equations, 31 (1979), pp. 53–98.
[20] J. Guckenheimer, *Singular Hopf bifurcation in systems with two slow variables*, SIAM J. Appl. Dyn. Syst., 7 (2008), pp. 1355–1377.
[21] J. Guckenheimer and H. M. Osinga, *The singular limit of a Hopf bifurcation*, Discrete Contin. Dyn. Syst., 32 (2012), pp. 2805–2823.
[22] E. Harvey, V. Kirk, H. Osinga, J. Sneyd, and M. Wechselberger, *Understanding anomalous delays in a model of intracellular calcium dynamics*, Chaos, 20 (2010), 045104.
[23] E. Harvey, V. Kirk, M. Wechselberger, and J. Sneyd, *Multiple timescales, mixed mode oscillations and canards in models of intracellular calcium dynamics*, J. Nonlinear Sci., 21 (2011), pp. 639–683.
[24] E. M. Izhikevich, *Neural excitability, spiking and bursting*, Internat. J. Bifur. Chaos Appl. Sci. Engrg., 10 (2000), pp. 1171–1266.
[25] J. Jalics, M. Krupa, and H. G. Rotstein, *Mixed-mode oscillations in a three time-scale system of ODEs motivated by a neuronal model*, Dyn. Syst., 25 (2010), pp. 445–482.
[26] C. K. R. T. Jones, *Geometric singular perturbation theory*, in Dynamical Systems, Lecture Notes in Math. 1609, R. Johnson, ed., Springer, New York, 1995, pp. 44–118.
[27] J. Keener and J. Sneyd, *Mathematical Physiology*, 2nd ed., Springer, New York, 2008.
[28] M. Krupa, N. Popović, N. Kopell, and H. G. Rotstein, *Mixed-mode oscillations in a three time-scale model for the dopaminergic neuron*, Chaos, 18 (2008), 015106.
[29] M. Krupa, N. Popović, and N. Kopell, *Mixed-mode oscillations in three time-scale systems: A prototypical example*, SIAM J. Appl. Dyn. Syst., 7 (2008), pp. 361–420.
[30] M. Krupa and P. Szmolyan, *Extending geometric singular perturbation theory to nonhyperbolic points—fold and canard points in two dimensions*, SIAM J. Math. Anal., 33 (2001), pp. 286–314.
[31] M. Krupa and M. Wechselberger, *Local analysis near a folded saddle-node singularity*, J. Differential Equations, 248 (2010), pp. 2841–2888.
[32] A. P. LeBeau, A. B. Robson, A. E. McKinnon, and J. Sneyd, *Analysis of a reduced model of corticotroph action potentials*, J. Theoret. Biol., 192 (1998), pp. 319–339.
[33] J. E. Lisman, *Bursts as a unit of neural information: Making unreliable synapses reliable*, Trends Neurosci., 20 (1997), pp. 38–43.
[34] G. Medvedev and J. Cisternas, *Multimodal regimes in a compartmental model of the dopamine neuron*, Phys. D, 194 (2004), pp. 333–356.
[35] E. F. Mishchenko, Yu. S. Kolesov, A. Yu. Kolesov, and N. Kh. Rhozov, *Asymptotic Methods in Singularly Perturbed Systems*, Monogr. Contemp. Math., Consultants Bureau, New York, 1994.
[36] A. I. Neishtadt, *Persistence of stability loss for dynamical bifurcations.* I, Differential Equations, 23 (1987), pp. 1385–1391.
[37] A. I. Neishtadt, *Persistence of stability loss for dynamical bifurcations.* II, Differential Equations, 24 (1988), pp. 171–176.
[38] J. Nowacki, S. Mazlan, H. M. Osinga, and K. Tsaneva-Atanasova, *The role of large-conductance calcium-activated K^+ (BK) channels in shaping bursting oscillations of a somatotroph cell model*, Phys. D, 239 (2010), pp. 485–493.
[39] H. M. Osinga and K. Tsaneva-Atanasova, *Dynamics of plateau bursting depending on the location of its equilibrium*, J. Neuroendocrinol., 22 (2010), pp. 1301–1314.
[40] J. Rinzel, *Bursting oscillations in an excitable membrane model*, in Ordinary and Partial Differential Equations, Lecture Notes in Math. 1151, Springer, Berlin, 1985, pp. 304–316.
[41] J. Rinzel, *A formal classification of bursting mechanisms in excitable systems*, in Proceedings of the International Congress of Mathematicians, Vols. 1, 2 (Berkeley, CA, 1986), A. M. Gleason, ed., AMS, Providence, RI, 1987, pp. 1578–1593.
[42] H. G. Rotstein, J. Opperman, T. White, and N. Kopell, *The dynamic structure underlying subthreshold activity and the onset of spikes in a model of medial entorhinal cortex stellate cells*, J.

Comput. Neurosci., 21 (2006), pp. 271–292.
[43] H. G. Rotstein, M. Wechselberger, and N. Kopell, *Canard induced mixed-mode oscillations in a medial entorhinal cortex layer* II *stellate cell model*, SIAM J. Appl. Dyn. Syst., 7 (2008), pp. 1582–1611.
[44] J. Rubin and M. Wechselberger, *The selection of mixed-mode oscillations in a Hodgkin-Huxley model with multiple timescales*, Chaos, 18 (2008), 015105.
[45] J. A. Sanders, F. Verhulst, and J. A. Murdock, *Averaging Methods in Nonlinear Dynamical Systems*, 3rd ed., Springer, New York, 2007.
[46] V. F. Safiulina, P. Zacchi, M. Taglialatela, Y. Yaari, and E. Cherubini, *Low expression of Kv7/M channels facilitates intrinsic and network bursting in the developing rat hippocampus*, J. Physiol., 586 (2008), pp. 5437–5453.
[47] J. V. Stern, H. M. Osinga, A. LeBeau, and A. Sherman, *Resetting behavior in a model of bursting in secretory pituitary cells: Distinguishing plateaus from pseudo-plateaus*, Bull. Math. Biol., 70 (2008), pp. 68–88.
[48] S. S. Stojilkovic, H. Zemkova, and F. Van Goor, *Biophysical basis of pituitary cell type-specific Ca^{2+} signaling-secretion coupling*, Trends Endocrinol. Metabol. 16 (2005), pp. 152–159.
[49] P. Szmolyan and M. Wechselberger, *Canards in $\mathbb{R}^3$*, J. Differential Equations, 177 (2001), pp. 419–453.
[50] P. Szmolyan and M. Wechselberger, *Relaxation oscillations in $\mathbb{R}^3$*, J. Differential Equations, 200 (2004), pp. 69–104.
[51] J. Tabak, N. Toporikova, M. E. Freeman, and R. Bertram, *Low dose of dopamine may stimulate prolactin secretion by increasing fast potassium currents*, J. Comput. Neurosci., 22 (2011), pp. 211–222.
[52] W. Teka, J. Tabak, and R. Bertram, *The relationship between two fast/slow analysis techniques for bursting oscillations*, Chaos, 22 (2012), 043117.
[53] W. Teka, J. Tabak, T. Vo, M. Wechselberger, and R. Bertram, *The dynamics underlying pseudo-plateau bursting in a pituitary cell model*, J. Math. Neurosci., 1 (2011), 12.
[54] W. Teka, K. Tsaneva-Atanasova, R. Bertram, and J. Tabak, *From plateau to pseudo-plateau bursting: Making the transition*, Bull. Math. Biol., 73 (2011), pp. 1292–1311.
[55] N. Toporikova, J. Tabak, M. E. Freeman, and R. Bertram, *A-type K^+ current can act as a trigger for bursting in the absence of a slow variable*, Neural Comput., 20 (2008), pp. 436–451.
[56] K. Tsaneva-Atanasova, H. M. Osinga, T. Rieb, and A. Sherman, *Full system bifurcation analysis of endocrine bursting models*, J. Theoret. Biol., 264 (2010), pp. 1133–1146.
[57] K. Tsaneva-Atanasova, A. Sherman, F. Van Goor, and S. S. Stojilkovic, *Mechanism of spontaneous and receptor-controlled electrical activity in pituitary somatotrophs: Experiments and theory*, J. Neurophysiol., 98 (2007), pp. 131–144.
[58] S. A. van Gils, M. Krupa, and P. Szmolyan, *Asymptotic expansions using blow-up*, Z. Angew. Math. Phys., 56 (2005), pp. 369–397.
[59] F. Van Goor, D. Zivadinovic, A. J. Martinez-Fuentes, and S. S. Stojilkovic, *Dependence of pituitary hormone secretion on the pattern of spontaneous voltage-gated calcium influx: Cell type-specific action potential secretion coupling*, J. Biol. Chem., 276 (2001), pp. 33840–33846.
[60] T. Vo, R. Bertram, J. Tabak, and M. Wechselberger, *Mixed mode oscillations as a mechanism for pseudo-plateau bursting*, J. Comput. Neurosci., 28 (2010), pp. 443–458.
[61] T. Vo, R. Bertram, and M. Wechselberger, *Bifurcations of canard-induced mixed mode oscillations in a pituitary lactotroph model*, Discrete Contin. Dyn. Syst., 32 (2012), pp. 2879–2912.
[62] M. Wechselberger, *Existence and bifurcation of canards in $\mathbb{R}^3$ in the case of a folded node*, SIAM J. Appl. Dyn. Syst., 4 (2005), pp. 101–139.
[63] M. Wechselberger, *À propos de canards (apropos canards)*, Trans. Amer. Math. Soc., 364 (2012), pp. 3289–3309.
[64] M. Wechselberger and W. Weckesser, *Bifurcations of mixed-mode oscillations in a stellate cell model*, Phys. D, 238 (2009), pp. 1598–1614.
[65] M. Zhang, P. Goforth, R. Bertram, A. Sherman, and L. Satin, *The Ca^{2+} dynamics of isolated mouse β-cells and islets: Implications for mathematical models*, Biophys. J., 84 (2003), pp. 2852–2870.